Evidence for Nb-Ta Occurrences in the Syn-Tectonic Pan-African Mayo Salah Leucogranite (Northern Cameroon): Constraints from Nb-Ta Oxide Mineralogy, Geochemistry and U-Pb LA-ICP-MS Geochronology on Columbite and Monazite

Periclex Martial Fosso Tchunte, Rigobert Tchameni, Anne-Sylvie André-Mayer, Hilaire Somtebda Dakoure, François Turlin, Marc Poujol, Emmanuel Negue Nomo, Alliance Nicaise Saha Fouotsa, Olivier Rouer

minerals

MDPI

Article

Evidence for Nb-Ta Occurrences in the Syn-Tectonic Pan-African Mayo Salah Leucogranite (Northern Cameroon): Constraints from Nb-Ta Oxide Mineralogy, Geochemistry and U-Pb LA-ICP-MS Geochronology on Columbite and Monazite

Periclex Martial Fosso Tchunte [1,*], Rigobert Tchameni [1], Anne-Sylvie André-Mayer [2], Hilaire Somtebda Dakoure [2], François Turlin [2], Marc Poujol [3], Emmanuel Negue Nomo [4], Alliance Nicaise Saha Fouotsa [1] and Olivier Rouer [2]

[1] Department of Earth Sciences, Faculty of Science, University of Ngaoundere, PO Box 454 Ngaoundere, Cameroon; rigotchameni@yahoo.fr (R.T.); nicsaha@yahoo.fr (A.N.S.F.)
[2] GeoRessources, Université de Lorraine, CNRS, F-54000 Nancy, France; anne-sylvie.andre@univ-lorraine.fr (A.-S.A.-M.); hilaire.dakoure@univ-lorraine.fr (H.S.D.); francois.turlin@univ-lorraine.fr (F.T.); olivier.rouer@univ-lorraine.fr (O.R.)
[3] University of Rennes, CNRS, Géosciences Rennes-UMR 6118, F-35000 Rennes, France; Marc.poujol@univ-rennes1.fr
[4] Department of Earth Sciences, Faculty of Science, University of Yaoundé I, P.O. Box 812, Yaoundé, Cameroon; emmanuelnegue@yahoo.fr
* Correspondence: fossopericlex@yahoo.fr; Tel.: +237-699-230-914

Received: 6 April 2018; Accepted: 25 April 2018; Published: 30 April 2018

Abstract: The Mayo Salah pluton, which is located in the North-Cameroon domain of Central African Bold Belt (CAFB), is emplaced as a laccolith in volcano-sedimentary schists of Poli series, and displays features of Rare-metal Granite (RMG). It is made of two main rock groups: (1) the metaluminous barren muscovite granite (MsG) and (2) the Nb-Ta bearing peraluminous leucogranite (MsL) which expresses four subtypes. The evolved Rare-element MsL is subalkaline, slightly peraluminous (ASI = 1.01–1.21), and it displays flat REE chondrite-normalized patterns with a strong negative Eu anomaly (Eu/Eu* = 0.02–0.20). It belongs to the peraluminous low phosphorus Rare-element Granites and L-type igneous rocks, as shown by the relatively low Zr/Hf (4.8–14) and Nb/Ta (1.4–9.0) ratios and the positive slope of the Zr-Hf-Nb-Ta profile in spider diagrams. The rare-element-bearing mineral is represented by columbite-group minerals (CGM) and other Nb-Ta-oxides (Nb-rutile and pyrochlore supergroup minerals). The CGM is classified as Mn-columbite, with Ta# and Mn# ratios increasing from core to rim. Two stages of mineralization are identified; the earliest stage (CGM-I) consists in scattered tabular or prismatic euhedral grains that were related to magmatic fractionation. The latest stage (CGM-II) is expressed as a Ta-rich Mn hydrothermal CGM episode represented as rims and/overgrowths around and/or as veinlet crosscutting CGM-I or in cleavage planes of muscovite. The U-Pb dating of columbite and monazite of the Mayo Salah leucogranite indicates a late-Neoproterozoic magmatic-hydrothermal mineralization event from 603.2 ± 5.3 to 581.6 ± 7.2 Ma, as consistent with both late D_2 to D_3 events that were recorded in the CAFB in Cameroon, and the associated continental collision environment. The Nb-Ta mineralization of the Mayo Salah pluton provides evidence for the presence of RMG in Northern Cameroon of CAFB, and its temporal association with the youngest period of metallogenic epoch of Nb-Ta-ore formation in Africa associated to Pan-African times.

Keywords: Mayo Salah; rare-metal granite; peraluminous leucogranite; Pan-African Nb-Ta mineralization; magmatic fractionation; U-Pb dating of columbite

1. Introduction

Rare-element deposits (Li, Be, Ta, Nb, Sn, W, and REE) are commonly found in magmatic rocks: peralkaline to pegmatitic peraluminous granites, carbonatites, and alkaline igneous rocks [1–5]. Enrichment of these lithophile elements may be directly linked to magmatic processes, as evidenced for the Beauvoir granite (French Massif Central [6–8]), Yichun granite of China [9,10], Czeck Podlesí granite [11,12]; or, magmatic-hydrothermal processes (e.g., [13–15].)

Rare-element granites have been divided in three categories by Linnen and Cuney [4]: (1) Peralkaline rare-element granites (ASI < 1, where ASI expresses the alumina saturation index, i.e., the molar (Al/[Na + K]) ratio) are characterized by very high abundances of F, REE, Y, Zr, Nb, high abundances of Th, Sn, Be, Rb, and U, high Nb/Ta, and low P (phosphorous) content, and are typically emplaced in anorogenic geotectonic settings; (2) Metaluminous to peraluminous low P rare-element granites have intermediate REE, Y, Zr, Hf, Th, and Pb contents. They correspond to the standard class of [16], the highly fractionated I- or A2-type granites of [17], or the magnetite-series granites of [18]. They occur in both post-orogenic and anorogenic geotectonic settings. The associated mineralization is mainly Nb-Ta-Sn as columbite-tantalite (Coltan) and cassiterite, and these granites have relatively low Zr/Hf and Nb/Ta ratios; (3) Peraluminous high P rare-element granites are characterized by extremely low REE (close to chondritic abundances), Y, Zr, Hf, Th, Sc, and Pb contents, and by the presence of Li-rich muscovite or lepidolite, Rb, and Cs contents are also generally very high. Because of their strongly peraluminous character, they are classically related to the S-type granites of [19].

The high-field strength elements (HFSE) Nb and Ta present both ionic charges and ionic radii that prevent them from being accommodated in the crystal lattice of common rock-forming minerals, and leave these elements in solutions. They are considered as incompatible elements during magmatic fractionation, and therefore, concentrations of these rare metals in silicate melts is related to small degrees of partial melting or to high degrees of fractional crystallization in evolved granitic and pegmatitic melts where their concentrations commonly increase until the saturation of the HFSE accessory phase, such as zircon, monazite, and/or Nb-Ta-bearing oxides [4,20,21].

Nb-Ta bearing oxide minerals (columbo-tantalite (coltan), pyrochlore) are used to establish fractionation evolution of rare-element granite [4,22–29]. Geochemical studies of oxides and various silicate minerals, as well as mineral zoning, used rare-metal as trace elements to reconstruct ore fractionation in granitic systems, and to characterize the closed- and open-system during magmatic to hydrothermal evolution [8,10,11,13–15,25,28,30–35].

Fractionation of Nb vs. Ta is commonly observed [3,36–38], with Nb usually highly concentrated in peralkaline granites [39] when Ta is mostly concentrated in peraluminous leucogranites and pegmatites [3,4,22,39,40]. The behaviour of the Nb and Ta elements drastically changes depending on melt composition and/or fluxing elements, like F, Li, P, and B [3,11,38,41–43].

Nb-Ta magmatic occurrences are reported worldwide, and the African continent is richly endowed with rare-metal bearing pegmatites and granites that are linked to numerous orogenic belts in Africa (Figure 1). Deschamps et al. [44] have compiled more than 1500 locations of known deposits of Ta and Nb in Africa. Melcher et al. [45] have characterized some local to regional differences in the mineralogy and geochemistry of the Ta-Nb-Sn bearing phases. Rare-metal granite (RMG) and pegmatite-bearing rare-element are described in several districts (Figure 1), from Archean to Mesozoic provinces [45–57]. Each of these periods of Ta-Nb-Sn ore formation is characterized by peculiar mineralogical and geochemical features that, when combined with geochronological constraints, allow for associating these provinces with magmatic episodes and a geodynamic environment: syn- to late-orogenic (e.g., West African Craton, Zimbabwe Craton), post-orogenic (Kibara Belt, Damara Belt,

Older Granites of Nigeria, Adola Belt of Ethiopia) and anorogenic (Younger Granites of Nigeria) ([45]; Figure 1).

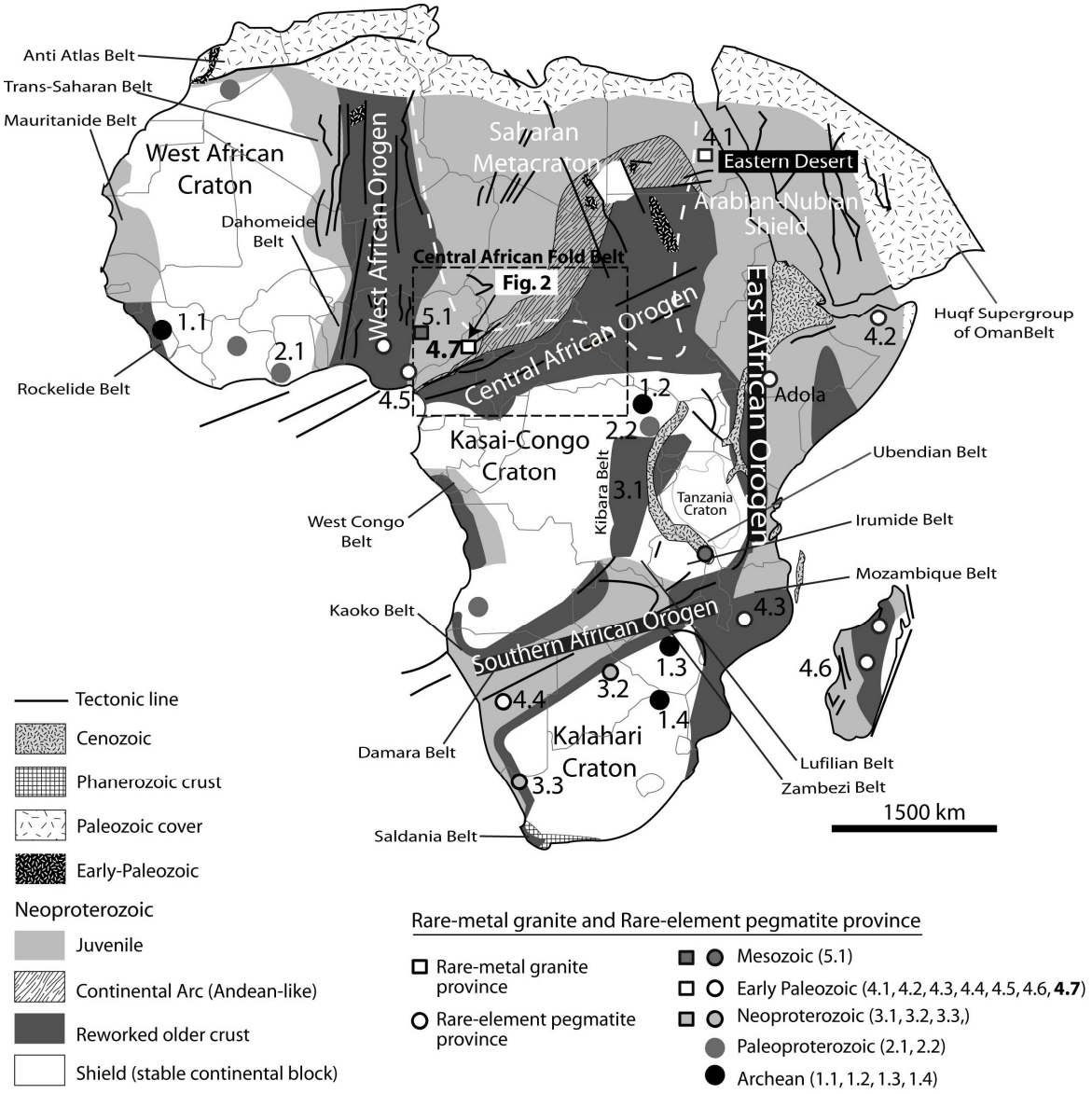

Figure 1. Location of the study area within the network of Pan-African belt, and the African rare-element pegmatite and rare-metal granite provinces (Modified from [45,58–60]. 1.1 Man Shield. 1.2 Congo Craton. 1.3 Zimbabwe Craton. 1.4 Kaapvaal Craton. 2.1 Birimian Province. 2.2 Kibalian in North-Eastern of Democratic Republic of Congo (DRC). 3.1 Kibara Belt. 3.2 Kamativi Schist Belt. 3.3 Orange River Belt. 4.1 Eastern Desert. 4.2 Adola Belt. 4.3 Alto Ligonha Province. 4.4 Damara Belt. 4.5 Older Granites (Nigeria). 4.6 Madagascar. 4.7 Mayo Salah in northern Cameroon domain of Central African Fold Belt. 5.1 Younger Granites (Nigeria).

To date, no Nb-Ta occurrences are described from the Poli region, which is located in the Northern Cameroon domain (NCD, Figure 2) of the Central Africa Fold Belt (CAFB). Early works in this area mainly focused on tectonic evolution and the associated magmatic activity in order to characterize the geodynamic evolution, especially in the Poli and the Tcholliré area (e.g., [61–70]). These studies also highlighted intrusive calc-alkali and peraluminous granites. This area is largely underexplored for its metallogenic potential, despite Cu mineralization that was noticed within this

volcano-sedimentary basin of Poli Group [71], and some U-bearing granite considered to be related to albitization processes [72–78].

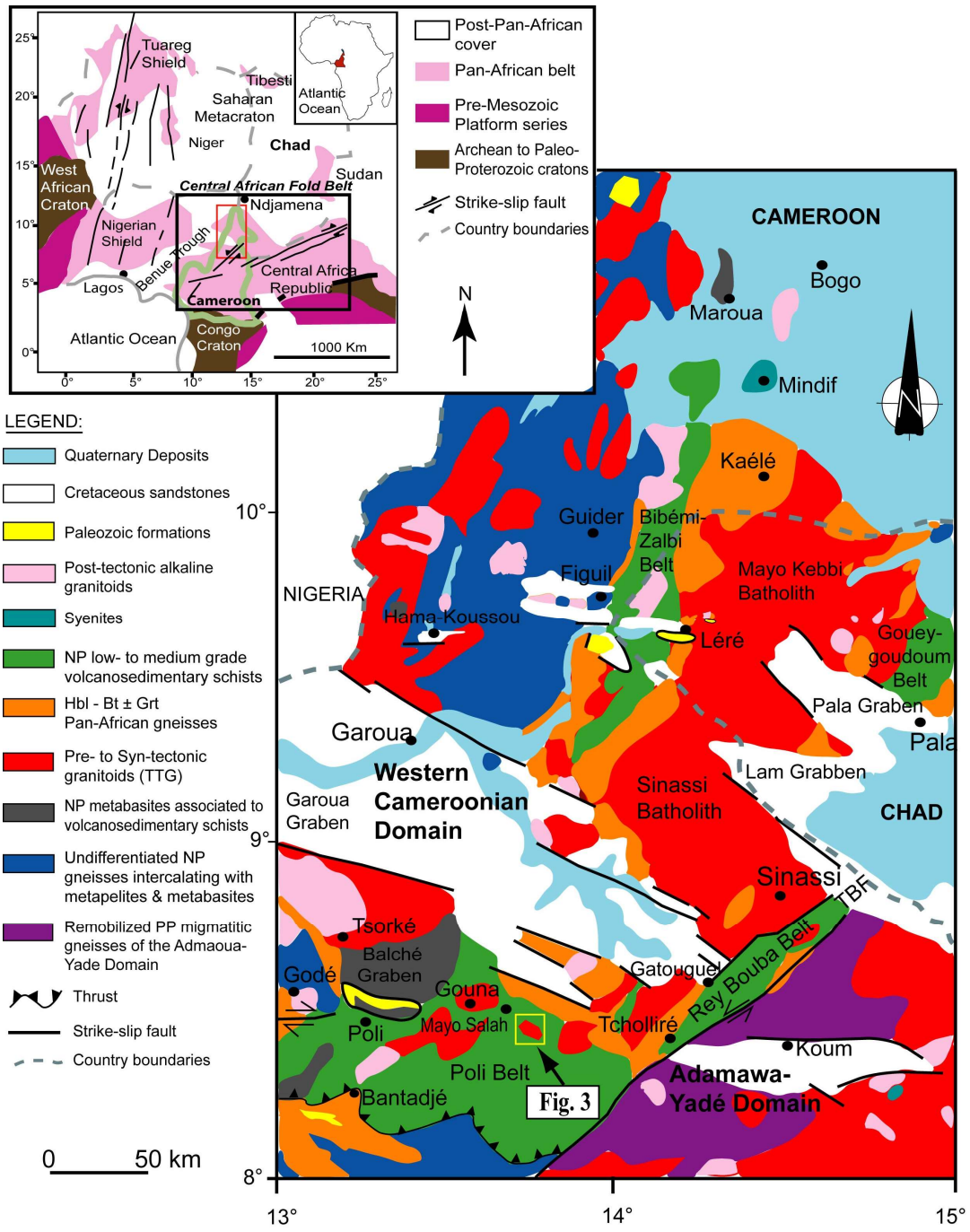

Figure 2. Geological sketch map of Northern Cameroon and Southwestern Chad. Abbreviations: NP = Neoproterozoic; PP = Paleoproterozoic; TBF = Tcholliré-Banyo Fault. Solid yellow square: study area (Figure 3). Inset: Location of the study area within the network of the Pan-African belts of West and Central Africa. Solid black square: Central African Fold Belt (CAFB); solid red rectangle: Figure 2. Modified after [63].

This paper presents an original geological description of the Mayo Salah leucogranite from the Poli region, North Cameroon (Figure 2). It provides evidence for the first rare-metal bearing granite that is described in this area through field observations, whole-rock geochemistry, textural features, and

mineralogy of Nb-Ta oxides-bearing minerals. Combining the geochemical and mineralogical features of the Mayo Salah leucogranite with U-Pb geochronological constraints on associated columbite and monazite minerals will allow for discussing the granite emplacement within the current knowledge of the geodynamic environment in this area during Pan-African times.

2. Geological Context

The Poli region belongs to the Northern Cameroon domain (NCD) of the Central Africa Fold Belt (CAFB) in Cameroon (Figure 2; [62–64,67–70,79]). This domain results from the collision between the Sahara metacraton [80,81] and the Adamawa-Yadé domain (AYD). Precambrian terrains of the NCD are made of the Neoproterozoic Poli Group that was intruded by Pan-African pre-, syn-, late-, and post-tectonic plutonic rocks. Whole-rock Sm-Nd, Sr-Nd isotopic dating, and zircon U-Th-Pb dating indicate that most of the gneissic and granitic rocks of this domain are Neoproterozoic in age with minor Paleoproterozoic to Mesoproterozoic records [66,68,70,72,82–84], contrasting with the abundant Paleoproterozoic ages that characterize the AYD [68,85–87]. The granitoids rocks of Poli group, the Sinassi batholith in Tcholliré area, and the neighboring Mayo Kebbi batholith in southwestern Chad, are considered as an unique Sinassi-Mayo Kebbi batholith [62,63,67,68,70,72,82,88–92] witnessing a Neoproterozoic continental magmatic arc setting of the Andean-type ([63,72]).

The Poli Group consists in well-preserved Neoproterozoic low, medium, to high grade schists of volcanic and volcano-sedimentary origin (metavolcanics are tholeiitic basalts and calc-alkaline rhyolites emplaced in a distensive crustal environment) that were intruded by several Pan-African granitoids. It is dominated by tectonically interleaved metavolcanic and metasedimentary rocks [79,90]. The metavolcanic units include sodic rhyolites and tholeiitic basalts when the metasedimentary units are composed of either purely volcanogenic clastic rocks (mainly tuffs) or variably reworked clastic rocks of dominantly intermediate composition (metagraywackes). Conglomerate layers are frequently observed in most of the sedimentary sequences (e.g., up to dm-size granitic pebbles in the clastic schists at Mayo Salah [70]. All of these rocks underwent a polyphased tectono-metamorphic evolution [69,89,91], comprising an early D_1 nappe tectonics deformed by open folding with sub-vertical axial planes (D_2). The medium- to high-pressure type metamorphism (garnet–kyanite–staurolite) reaches anatexis in lower crustal levels [82,93]. The ca. 830 Ma rhyolite at Goldyna and the concordant zircon ages of ca. 920 and ca. 780 Ma recorded in magmatic rocks from neighboring area (e.g., Goldyna metarhyolite and trondhjemitic pebbles) correspond to the ages of the underlying volcanic sequence [67,70,94]. On the basis of ion microprobe U-Pb dating of zircons from volcano-sedimentary sequences, the depositional age of the Poli basin is constrained between ca. 700 and ca. 665 Ma; detrital sources comprise ca. 920, 830, 780, and 736 Ma inherited magmatic zircons. This basin is considered to be pre- to syn-collisional developed upon, or in the vicinity of, young magmatic arcs [70,90,95].

Several Pan-African granitoids have been identified and investigated in the NCD, and then correlated to its neighboring counterparts in southwestern Chad and eastern Nigeria (Figure 2). Three main generations of these plutonic rocks are discriminated, based on available geological, geochemical and geochronological data. (1) The oldest stage emplaced before the transcurrent tectonic and the regional migmatization, and it includes pre- to syn-collisional granitoids consisting mainly of calc-alkaline basic to intermediate plutons that were dated at ca. 740–630 Ma. The North Cameroon orthogneiss, the Sinassi, and the Mayo Kebbi batholiths belong to this plutonic group [63,66–68,84,91,92,94]; it is likely interpreted as a continental magmatic arc that is related to a subduction zone (Figure 2); (2) The most abundant stage is composed of late- to post-collisional granitoids as they are associated with the main phase of collision, transcurrent shear zones, and migmatization. They are made up essentially of basic to felsic plutons. Two subgroups are distinguished and dated, respectively, at (2a) ca. 620–600 Ma; and, (2b) ca. 590–560 Ma [66–69,72,83,91,94]; (3) The youngest stage includes post-tectonic alkaline

granitoids that were emplaced at ca. 550–530 Ma (Godé granitic massif, [69,96]), which are related to crustal extension.

3. Analytical Methods

Twenty-one representative hand-samples were collected on the Mayo Salah pluton for polished thin sections, whole-rock geochemistry, mineral chemistry, and geochronology.

3.1. Whole-Rock Geochemistry

The selected samples were crushed in a jaw crusher and were powdered in an agate mill to avoid contamination. The whole-rock compositions were measured using inductively coupled plasma atomic emission spectrometry (ICP-AES) for major elements, and inductively coupled plasma mass spectrometry (ICP-MS) for trace elements at the SARM (Service d'Analyse des Roches et des Minéraux, CRPG-CNRS, Nancy, France). Sample preparation, analytical conditions, and limits of detection are detailed in Carignan et al. [97].

3.2. Imaging and Mineral Chemistry

The textures of rare-element minerals and the associated mineral assemblage were observed on polished thin sections, using the backscattered electron mode (BSE) of Hitachi S4800 scanning electron microscope (SEM), equipped with an EDS spectrometer at GeoRessources laboratory (Nancy, France) to characterize the paragenetic assemblages of the samples.

The mineral chemical compositions were obtained using an electron probe microanalyser (EPMA) CAMECA SX-100 at GeoRessources laboratory (Nancy, France). We present here the results of ca. 125 in-situ EPMA analyses that were obtained from different single crystals of Nb-Ta oxide minerals. Major and minor elements are expressed in weight per cent oxides (wt %). The operating conditions for the quantitative analyses were set at 15 kV accelerated voltage, 12 nA beam current, peaks, and background counting time set up to 10 s and 5 s for major element and trace elements, such as Sc, W, Y, U, Th, respectively; spot size of 1 μm^2, applying the ZAF data correction (Z for atomic number effect; A for self absorption effect, and F for Fluorescence effect). Both metals and compounds were used as standards.

3.3. U-Pb Dating of Columbite and Monazite using Laser Ablation-Inductively Coupled Plasma-Mass Spectrometry (LA-ICP-MS)

Columbite and monazite grains have been extracted from two hand-samples of leucogranite (MS35c and MS38) using conventional procedure of densimetric, magnetic and bromoform density separation at GeoRessources laboratory (STEVAL experimental station). The columbite and monazite grains were handpicked under a binocular microscope and were mounted in epoxy resin. These epoxy mounts were polished using standard methods and were imaged via BSE using Hitachi S4800 SEM. For zoned columbite grains, only the cores were analyzed because the rims were too thin to be analyzed (Figures 13a and 14a). U-Pb dating of columbite and monazite was conducted by LA-ICP-MS at Géosciences Rennes (France) using an ESI NWR193UC Excimer laser coupled to a quadripole Agilent 7700X ICP-MS. During the course of an analysis, the signals of ^{204}(Pb + Hg), ^{206}Pb, ^{207}Pb, ^{208}Pb, ^{232}Th, and ^{238}U masses are acquired. No common Pb correction was applied, owing to the large isobaric interference with Hg. The ^{235}U signal is calculated from ^{238}U on the basis of the ratio $^{238}U/^{235}U = 137.88$. A single analysis consisted of 20 s of background integration, followed by 60 s integration with the laser firing, and then 10 s delays to wash out the previous sample. For more information on the settings of the instrument, see Ballouard et al. [98] and supplementary Table S1. Spot diameters of 30 µm for columbite and 10 µm for monazite associated with repetition rates of 4 Hz (columbite) and 2 Hz (monazite) with a laser fluency of 8.8 J/cm^2 were used.

Data were corrected for U-Pb and Th-Pb fractionation, and for the mass bias by standard bracketing with repeated measurements of the GJ-1 zircon standard (columbite; [99]) or the Moacir

monazite standard (monazite; [100]). Repeated analyses of the 91,500 zircon standard (1066.3 ± 8.9 Ma (n = 6); [101]) or the Manangoutry monazite standard (545 ± 10 Ma (n = 9); [102]) treated as unknowns were used to control the reproducibility and the accuracy of the corrections.

Data reduction was carried out with the GLITTER® software package developed by the Macquarie Research Ltd. (Sydney, Australia) [103]. Concordia ages and diagrams were generated using Isoplot/Ex [104]. All of the errors that are given in supplementary Tables S1, 3, and 4 are listed at one sigma, but where data are combined for regression analysis or to calculate weighted means, the final results are provided with 95% confidence limits.

4. Results

4.1. The Mayo Salah Pluton: Field Relationships, Structural Constraints and Macroscopic Petrographic Features

Several plutons are outcropping in the Mayo Salah region, among them, the Mayo Salah pluton (MSP) expressing the mineralogical character of rare-metal granites (Figures 2 and 3).

4.1.1. Field Relationships and Macroscopic Features

The MSP (3 km long and 2 km wide) intrudes the schists of the Poli Group with a concordant contact (Figure 3). The pluton outcrops from North to South as four parallel and elongated E-W flat hills, with altitudes that were ranging between ca. 340 and 410 m. The pluton has a NNW-SSE elliptic shape and more or less homogeneous petrographic types in its north and south boundaries. Macroscopic and detailed field observations (Figures 4 and 5), which were based specifically on the color index and the granulometry of the samples, allow for the distinction of two main groups: (1) the porphyric muscovite granite (MsG) and (2) the muscovite leucogranite (MsL). The transition between the MsG and the MsL is outlined by the change of mineralogical composition, color index, and outcropping mode.

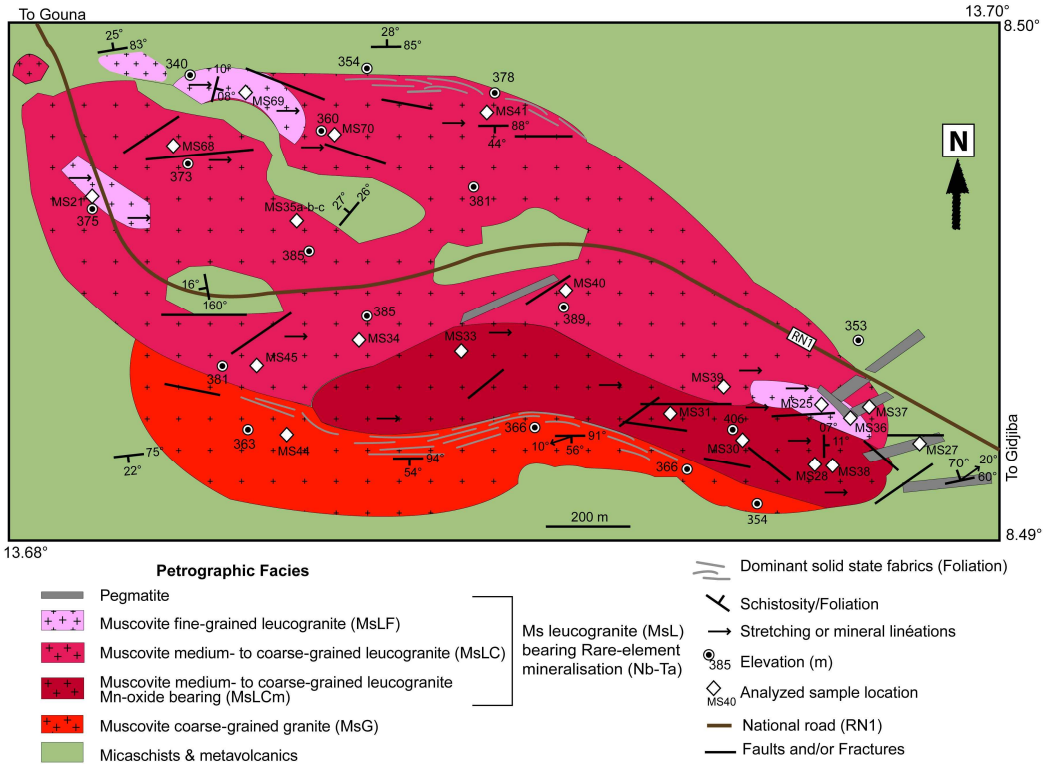

Figure 3. Geological map of the Mayo Salah pluton (MSP), showing the investigated rare-metal granite and the location of analyzed samples.

The Muscovite granite (MsG) represents 1/5 of the area of the MSP (Figure 3). This facies outcrops in the southern part of the pluton. It presents a subvertical foliation with stretching lineation (Figure 4a). MsG is mesocratic, porphyric medium- to coarse-grained made of quartz, muscovite, plagioclase ± biotite ± orthose (Figure 4b,c). The rock may locally display a preferred orientation of minerals, which were mostly underlined by the general organization (sub-)parallel to the (001) cleavage planes of muscovite (Figure 4b).

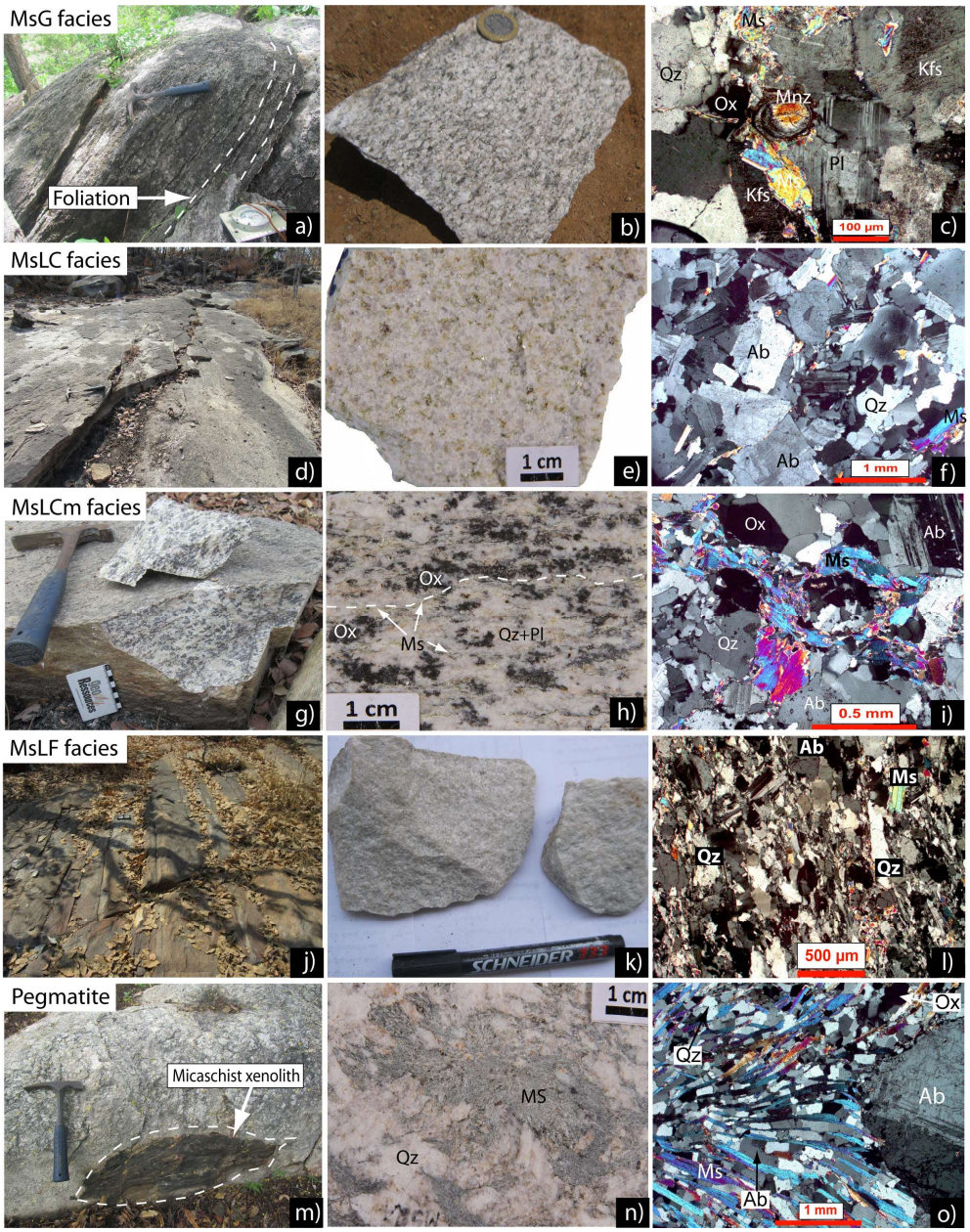

Figure 4. Photographs of the two main group rocks of Mayo Salah pluton. Muscovite-granite (MsG) and muscovite-leucogranite with its four subtypes (MsLC, MsLCm, MsLF, and Pegmatite, abbreviation code is the same as in Figure 3): (**a**,**d**,**g**,**j**,**m**) Field photographs. Note: hammer handle indicates the north direction; (**b**,**e**,**h**,**k**,**n**) Hand-samples of MsG, MsLC, MsLCm, MsLF, and Pegmatite, respectively; (**c**,**f**,**i**,**l**,**o**) Photomicrographs in cross-polarized light of each samples showing representative textures of MsG, MsLC, MsLCm, MsLF, and Pegmatite, respectively. Abbreviations: Qz: quartz, Ms: muscovite, Pl: plagioclase, Kfs: K-feldspar, Mnz: monazite, Ox: oxide, Ab: albite.

The muscovite leucogranite (MsL) is the main facies of the MSP, as it represents about 4/5 of the area (Figure 3). It is generally made of quartz, feldspar, muscovite, and opaque minerals. A distinction that is based on the color index and texture, the size of minerals, and the proportion of oxide minerals allowed for the distinction of the four following subgroups:

(i) Porphyric medium- to coarse-grained muscovite leucogranite (MsLC) is the dominant leucogranite subgroup and it represents most of the northern part of the pluton (Figure 3), and it displays progressive contact with the MsG and MsLCm in its southern limit (see below in the text). The outcrops are generally highly fractured blocks and flagstones (Figure 4d). The rock is leucocratic medium- to coarse-grained made of quartz, plagioclase, muscovite, ±Nb-Ta oxides, and ±garnet (Figure 4e,f). At the transition with the MsLCm facies, the MsLC facies displays an abundant and disseminated concentration of Mn-oxide minerals and miarolitic cavities that are rounded by Mn-oxide.

(ii) Porphyric medium- to coarse-grained muscovite leucogranite, Mn-oxide-bearing (MsLCm), is much observed on the highest hill in the southeast sector of the pluton (Figure 3). It displays a sharp contact with the MsLC. The major difference with the MsLC is its mesocratic color index, due to the high proportion of the disseminated flecks of Mn-oxide (Figure 4g–i).

(iii) Microgranular fine-grained muscovite leucogranite (MsLF) (<1/5 of the pluton) consists of many pockets of ≤10 m of outcrops (Figure 4j), which are usually at the borders of other leucogranites or are in contact with the host rock. It is leucocratic (Figure 4k) and fine-grained made of quartz, feldspar, and muscovite, with a preferred orientation of muscovite (Figure 4l). The texture is microgranular or aplitic at the contacts with the host rock or with the pegmatite.

(iv) Pegmatites (Peg) outcrops as large veins that are discontinuously distributed in the Ms-leucogranite and crosscut the intruded schists, they also contain xenoliths of schists (Figures 4m and 5f). It varies in thickness from <1 to ca. 15 m and average 30 m in length. It is characterized by quartz, feldspar, and K-feldspar megacrysts, with flakes of muscovite, plagioclase and Nb-Ta-oxide in interstice (Figure 4n,o). Accessory Mn-oxide occurs in fractures and in cleavage cracks.

4.1.2. Structural Features

The lithologies that were intruded by the Mayo Salah pluton have a shallow-dipping schistosity with various directions (N26–N85) and dip oriented towards N and NW (up to 28°). This schistosity is visible on outcrops that are located along road trenches (Figure 5a) and in river beds at the North of the pluton (Figures 3 and 5b,c). The schistosity is delineated by internal micro-fold with axial planes that are parallel to the schistosity plane (Figure 5d). In the southern part of the pluton, this shallow-dipping schistosity (up to 16° towards W) displays a different orientation and is weakly folded. An enclave of schist is also visible in some rocks of the MSP (Figures 4m and 5e,f).

The MSP is weakly deformed. A pervasive solid state deformation has been observed in its borders that is emphasized by subvertical foliation with stretching lineation (Figure 5). The foliation is locally highlighted by quartz-feldspar veins (Figure 5g). The central part of the pluton does not show any sign of deformation but the local mineral lineation (N75E–N110E), witnessed by muscovite and quartz are observed in some facies (Figure 5h). This deformation is progressive and it decreases from the border towards the core of the pluton. This is typical for composite, multiphase intrusions. In the borders, the foliation is oriented E-W with southbound plunges (up to 56°), which are underlined by fractures and quartz-feldspar veins (Figures 4a and 5i,j). The limit between the pluton and the host rock at the northern boundaries displays identic fabric between the schist and the MsL and mixture features where the structures of the hosting rocks are even visible (Figure 5e,f). This points to a northbound vergence of the pluton with structures straightened at its southern boundaries (Figures 4a and 5i) that lie down progressively northbound (Figure 5j). In the central part of the pluton, mainly in the MsG, MsLCm, and MsLF, the flagstones have variable directions with very shallow-dipping fabrics (up to 12°), with a magmatic flow and mineral lineation (E-W) that is underlined by the preferred

orientation of (001) muscovite cleavage planes and feldspars (Figure 5h). Many fractures assigned to fault/fracture (Figure 5k) and conjugate sinistral/dextral shearing mainly NE-SW (N50E–N70E), E-W (N80–N90E) and WNW-ESE (N110E–N150), affect these rocks and some quartz veins (Figure 5l,m). The quartz has undulose extinction, feldspars are broken or sheared and are filled by muscovite or/and quartz (Figure 5n), and muscovite is kinked (Figure 5o). All of these elements provide evidence that this pluton underwent a tectonic event that was less pronounced in the core of the plutons than at its boundaries that display a dominant solid state deformation.

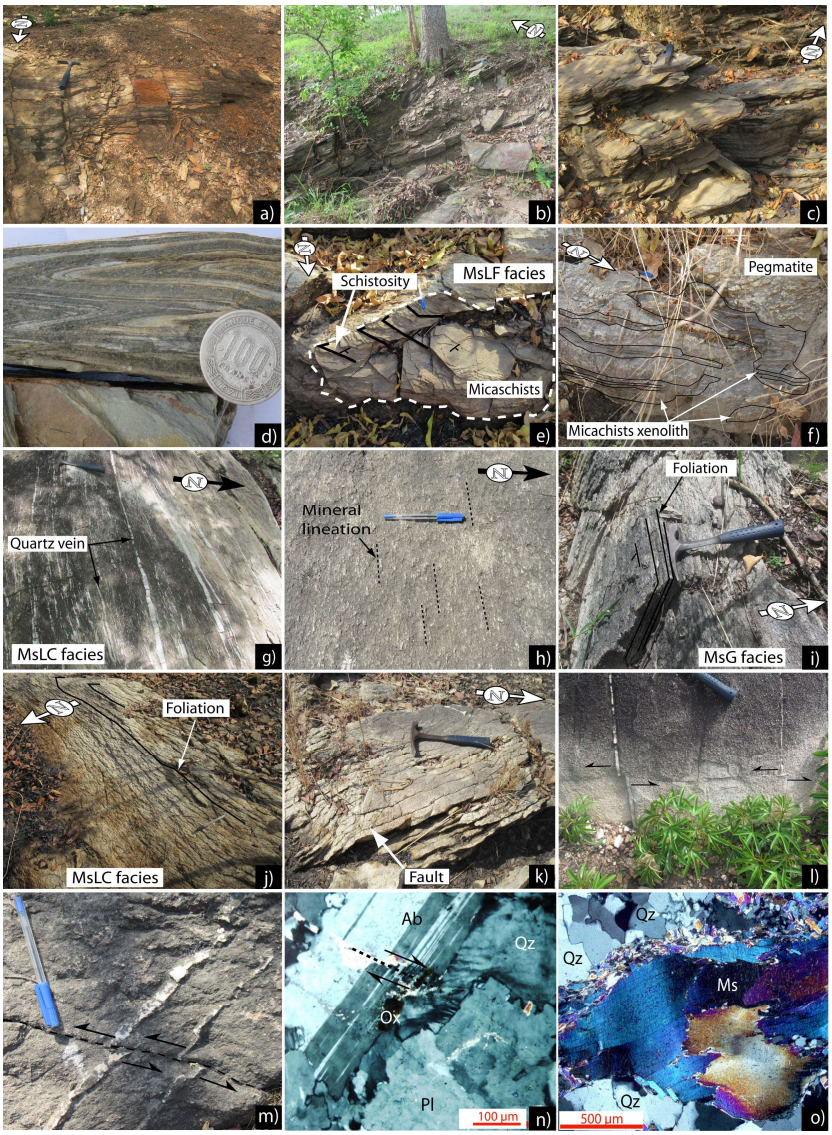

Figure 5. Field photographs showing the structural features of the Mayo Salah pluton: (**a**–**c**) Shallow-dipping schistosity in the micaschists basement; (**d**) Flat folding in a hand sample of schists; (**e**,**f**) Northern border of the pluton with mixture between micaschists and MsLF facies and preservation of fabrics in the micaschists; (**g**) Quartz veins underlining the foliation in the leucogranite facies; (**h**) Outcrop of MsLCm with preferred orientation (E-W) of quartz and muscovite; (**i**) Subvertical foliation at the southern boundary of the pluton (MsG facies); (**j**) Shallow-dipping foliation in the LFG facies at the northern boundary of the pluton; (**k**) Fault in outcrop of MsLC; (**l**,**m**) Sinistral shearing affecting quartz veins in outcrop of MsG and MsLC, respectively; and, (**n**,**o**) Microstructures of sheared plagioclase and kinked muscovite related to deformation (muscovite-leucogranite facies). Abbreviations: Ab: albite, Ms: muscovite, Ox: oxide, Pl: plagioclase, Qz: quartz.

4.2. Mineralogical Assemblages of the Main Facies

A summary of the mineral assemblages that were observed in the different facies of the Mayo Salah pluton is proposed in Table 1. The MSP granites are mainly composed of quartz, plagioclase, muscovite, K-feldspar, numerous oxides, like Mn-oxide (Figure 4g–i), and Nb-Ta oxide, like columbite-tantalite (Coltan, Figure 4c,f,i,l,o, Figures 6 and 7). A second generation of minerals consists in interstitial quartz, muscovite, feldspars, oxide minerals, and F-rich calcite (Figure 4c,i and Figure 6).

Table 1. Main mineral assemblage type (ordered by abundance) of the various facies of the Mayo Salah pluton.

Petrography (Facies)	Subgroup	Common Minerals	Minor Minerals	Rare Minerals
Muscovite granite (MsG)	-	Quartz Muscovite Plagioclase Orthose	Microcline Zircon Titanite Fe-Oxide	Biotite Epidote Myrmekyte Garnet Allanite
Muscovite Leucogranite (MsL)	MsLC (Porphyric medium- to coarse-grained muscovite leucogranite)	Quartz Muscovite Plagioclase Microcline	Nb-Ta oxide Garnet Fluorite Mn-oxide	Cassiterite Wolframite Pyrochlore Zircon Fe-oxide Monazite
	MsLCm (Porphyric medium- to coarse-grained muscovite leucogranite, manganese oxide-bearing)	Quartz Muscovite Plagioclase Calcite Mn-oxide Microcline	Pyrochlore Garnet Fluorite F-calcite Fe-oxide	Rutile Nb-Ta oxide Wolframite Cassiterite Zircon Monazite
	MsLF (Microgranular fine-grained muscovite leucogranite)	Quartz Muscovite Plagioclase Microcline	Nb-Ta oxide Garnet	Epidote Mn-oxide Fluorite
	Peg (Pegmatite)	Quartz Muscovite Plagioclase Microcline Mn-oxide	Garnet Fe-oxide	Nb-Ta oxide Zircon

Quartz is expressed as subeuhedral megacrysts with various sizes (up to 1 mm) in coarse samples (Figure 4c,f,n), and as medium crystals (up to 300 µm) in fine- to medium-grained samples (Figure 4i). The second generation of quartz is expressed as interstitial grains. Plagioclase is albite, and it is mostly expressed as groundmass, like quartz. It is made of coarse euhedral megacrysts (Figure 4c-f,h,i,k,n), with common inclusions of quartz, secondary muscovite, F-calcite, and oxide minerals (Figures 4c and 6b,d,g). A second generation of plagioclase is expressed as subeuhedral interstitial fine minerals. K-feldspar is microcline and garnet is spessartine, locally altered in MsLCm facies and pegmatites.

The MsL subgroups express different features in their texture, mineral compositions, and distribution of rare-element mineralization. The MsLC and MsLF subgroup are the Nb-Ta-richest oxide-bearing minerals with little proportions of fluorite and monazite. Its texture is porphyric (Figure 4c,f,i,l and Figure 6). Pegmatites are rich in Mn-oxide, but host few Nb-Ta oxide minerals. The MsLCm subgroup is rich in fluorite and monazite in miarolitic cavities; pyrochlore is abundant in this subtype, with calcite, F-calcite and Mn-oxide; Nb-Ta bearing-minerals being less abundant (Figure 6g,h). The Nb-Ta mineralization is spatially zoned in the MSP with the increase of Nb-Ta bearing-oxide minerals from the South to the North: (1) the barren MsG; (2) the least mineralized MsLCm in coltan but rich in other Nb-Ta oxide, like metamict pyrochlore and Nb-rutile; (3) the most mineralized subgroups, MsLC and MsLF facies; and (4) pegmatites. This distribution of Nb-Ta bearing-oxide minerals is consistent with the petrographic zonation of the MSP (Figure 3).

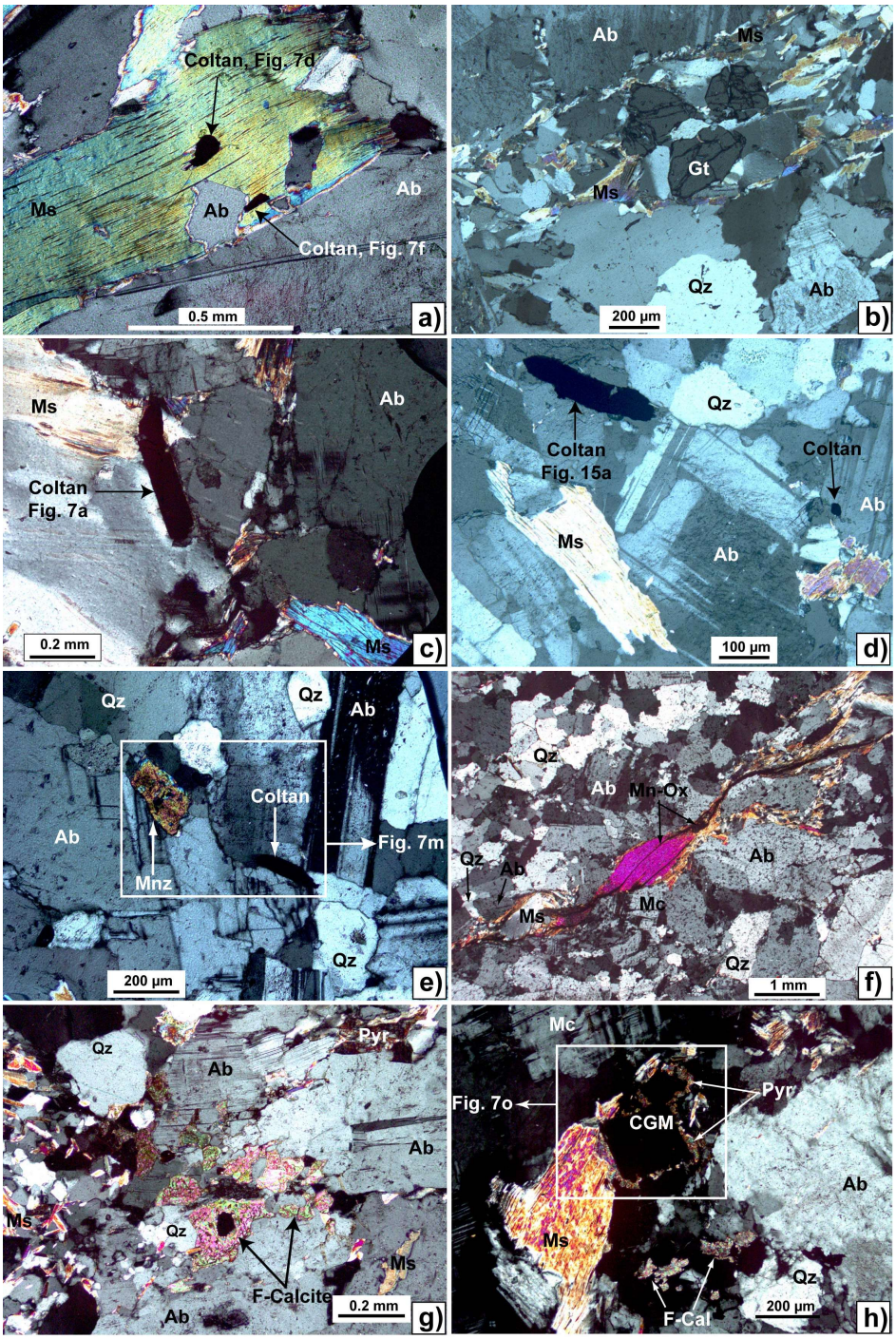

Figure 6. Photomicrographs under cross-polarized light showing textural relationships characterizing rare-metal minerals of the different facies of muscovite-leucogranite of Mayo Salah pluton: (**a**) muscovite crystal displaying inclusions of columbo-tantalite (coltan) and albite in Muscovite coarse-grained leucogranite facies (MsLC); (**b**) porphyric texture in MsLC facies; (**c**–**e**) porphyric texture showing Nb-Ta oxides minerals; (**f**) porphyric texture in MsLCm facies with preferred orientation of muscovite. Note the abundance of Mn-oxide along the cleavage plane of muscovite and in foliation plane; (**g**) Inequigranular texture in MsLCm showing pyrochlore minerals and fluoro-calcite sometimes as inclusions in feldspar; and, (**h**) crystal of columbite, surrounded by pyrochlore minerals. Abbreviations: Qz: quartz, Ms: muscovite, Ab: albite, Mc: microcline, Gt: garnet, Mnz: monazite, Pyr: pyrochlore, coltan: columbo-tantalite, Mn-Ox: manganese oxide, F-calcite: fluoro-calcite, CGM: columbite-group mineral.

4.3. Habit, Distribution, Texture and Compositions of Rare-Element-Bearing Minerals

The most common rare-element-bearing mineral that was observed in the Mayo Salah pluton corresponds to columbite-group mineral (CGM), especially columbite-tantalite so called coltan, the most important group of Nb-Ta minerals [24]. In addition, other phases hosting Nb-Ta are present such as other Ta-Nb-oxides (TNO), like Nb-rutile and pyrochlore supergroup minerals (Figure 6h). All these rare-element-bearing minerals are expressed either as scattered prismatic, tabular minerals or small needle-like grains, generally in association with muscovite and albite (Figure 6). Their size varies between 20 and 400 µm long (Figure 6a,c–e,h).

4.3.1. Columbite-Group Mineral

CGM is observed in varying abundance in the silica matrix of all MsL subgroups, commonly in MsLC and MsLF, fewer in MsLCm and pegmatite, and never in MsG (Figure 6). BSE images reveal that CGM are weakly heterogeneous, with a sharp but concordant rim zone, as is consistent with a simple core-rim normal zoning (Figure 7 and Figure 13a). In a simple type zoning patterns, we distinguish progressive and rarely patchy and oscillatory zoning in some coltan grains. The patchy zoning is observed in MsLCm and MsLC facies (Figure 7l and Figure 14a). The progressive zoning appears mainly in all facies, and consists of Nb-rich darker (core) and Ta-rich brighter (rim) areas (Figure 7 and Figure 13a). It is consistent with magmatic fractionation in agreement with other worldwide studies [28,105]. CGM-I constitutes the earliest stage of mineralization. They occur as scattered tabular or prismatic euhedral grains up to 400 µm long, disseminated between quartz, plagioclase, muscovite, and microcline (Figures 6c–e and 7i,m,o). Another generation of CGM-I occurs as small needle-like grains and subeuhedral to anhedral grains in primary muscovite and albite (Figure 6a,d), disseminated/interstitial with/within a second generation of muscovite and plagioclase. These minerals are fractured and may exhibit inclusions of albite, zircon (Figure 7a,c,g,m,n), and uraninite or thorite (Figure 14a). CGM-II corresponds to the late stage of mineralization. It is characterized by a zonation around the minerals and/or veinlet (brighter area) in fracture of CGM-I or in cleavage plane of muscovite (Figure 7, Figures 13a and 16). The Ta# and Mn# increase from core to rim of the minerals. It is most observed the MsLC facies of the MSP (Figure 8).

The composition of the core of coltan (CGM-I), which is characterized by various shades of grey, display some differences with the composition of the rim (CGM-II), characterized by various shades of bright. The geochemistry in all of the subgroups of investigated columbite-Mn presents the following range of: 9.68–17.74 wt % MnO; 1.55–9.23 wt % FeO; 31.84–72.33 wt % Nb_2O_5; 5.29–46.59 wt % Ta_2O_5. In addition, small amounts of TiO_2 (0.00–2.74 wt %), SnO (0.00–0.50 wt %), UO_2 (0.00–0.80 wt %), Y_2O_3 (0.13–0.83 wt %), and Sc_2O_3 (0.00–0.16 wt %) were detected (Supplementary Materials Tables S2–S4). These compositions of CGM are plotted in the columbite quadrilateral diagram (Figure 8) and the representative results are given in Supplementary Materials Tables S2–S4. All of the CGM of different subgroup of leucogranite of the MSP express a manganocolumbite (columbite-Mn) composition, with high Mn# ratio varying in a small range from 0.52 to 0.90 and low Ta# varying widely from 0.04 to 0.47 (Figure 8). They display a wide range of compositions with an evolutionary trend from core to rim, with an increase of Mn and Fe versus a decrease of Nb and Fe. The core zones of the crystals have Ta# values of <0.19, while the rims always have higher Ta# values of <0.47, and Ta# ratios increase continuously from the core to the rim of the crystals in the most evolved facies (MsLC and MsLF, Figure 8).

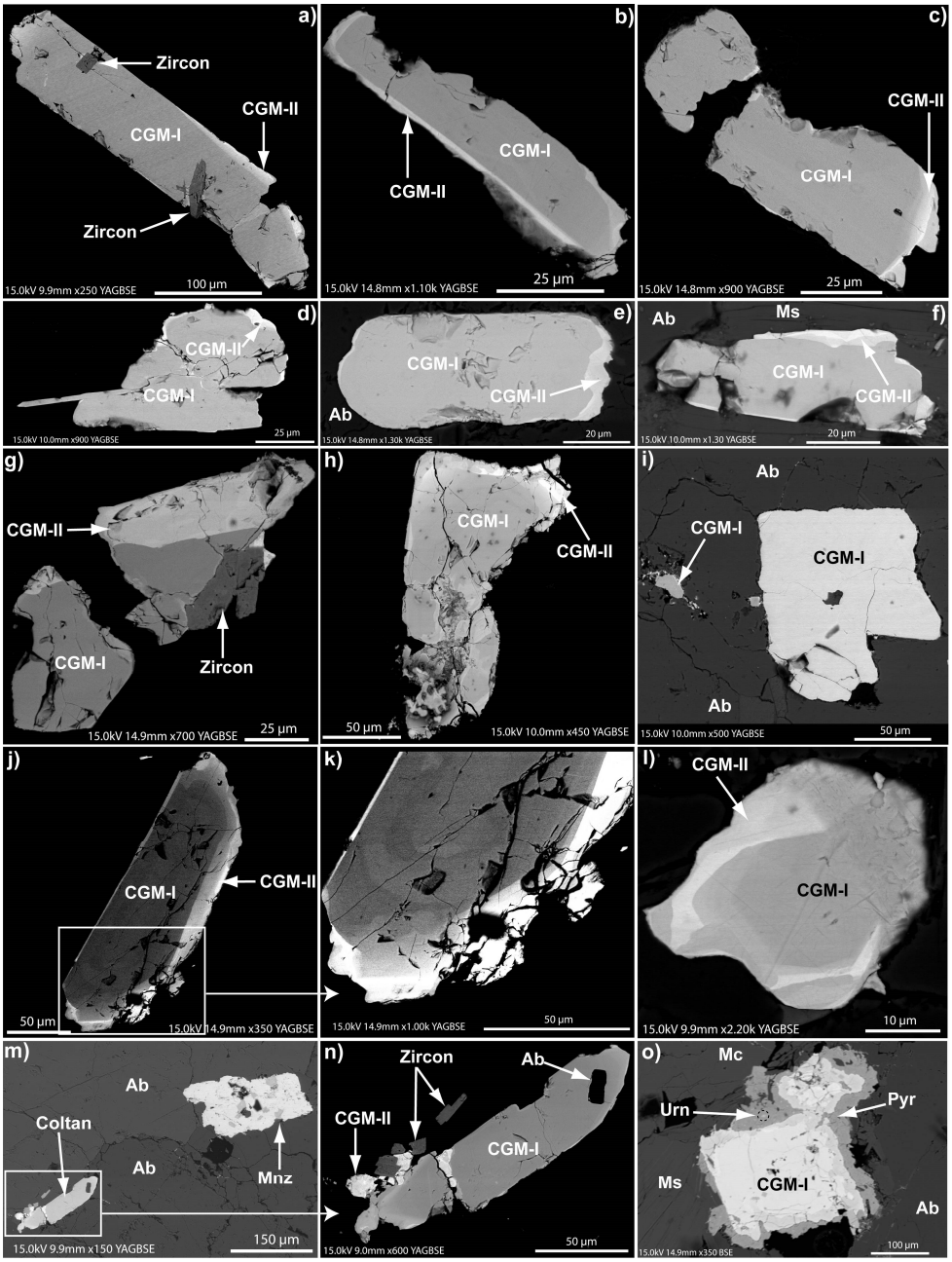

Figure 7. Backscattered electron mode (BSE) images showing the common occurrences, texture and zonation of Columbite-group minerals (CGM). Note that they are euhedral to subeuhedral, sometimes cracked with inclusions of plagioclase and zircon. The zonation is associated with varying abundances of Nb (gray) over Ta (various shades of bright): (**a**) Euhedral prismatic crystal of CGM, with simple zonation. The mineral is fractured with inclusions of albite and zircon; (**b**–**e**) CGM with simple zoning. The needle-like crystal in Figure 7d is an inclusion within the muscovite (see Figure 6a); (**f**) Inclusion of CGM in muscovite (see Figure 6a) displaying oscillatory zoning; (**g**,**h**,**l**) Patchy zoning in some subeuhedral tabular crystal of CGM; (**i**) Crystal of primary columbite without zonation outlining the magmatic state of mineralization; (**j**,**k**) Crystal of CGM displaying simple progressive and oscillatory zoning type; (**m**) Association of CGM and monazite in silicate matrix (see Figure 6e), details of CGM is given in Figure 7n, note the inclusion of albite in this mineral, the little zonation and the association of zircon with CGM-II; and, (**o**) Euhedral crystal of CGM-I, rimmed by pyrochlore minerals that are rich in uraninite inclusions. Abbreviations: Ab: albite, Ms: muscovite, Mc: microcline, Mnz: monazite, Urn: uraninite, CGM-I: primary columbite-group mineral, CGM-II: secondary columbite-group mineral.

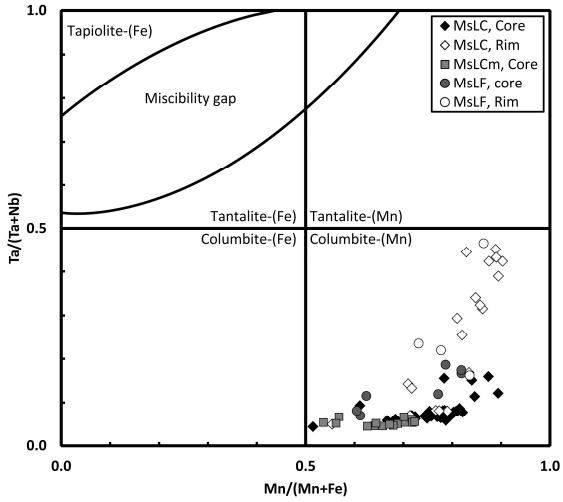

Figure 8. Ta/(Nb + Ta) vs. Mn/(Mn + Fe) compositional diagram for columbite-group minerals.

4.3.2. Other Ta-Nb Oxide Minerals (TNO)

The other TNO minerals in the MSP include Nb-rutile and pyrochlore-supergroup minerals, with uncommon compositions. They are more abundant in the MsLCm facies.

The investigated rutile is Nb-rich without zonation. They occur as subeuhedral or anhedral oxide (up to 650 µm long) in muscovite flakes. The textural pattern of the examined Nb-rutile witness geochemical heterogeneities, suggesting that nano- to microscopic grains of pyrochlore might be present as inclusions in the crystal.

A pyrochlore-supergroup mineral occurs as euhedral to subeuhedral grain in silicate matrix or as inclusions in muscovite. The grains are mainly metamict with common inclusions of uraninite and thorite. Other phases appear around CGM-I (Figures 6h and 7o). The wide range of textural patterns of TNO and their relation with CGM is consistent with hydrothermal mineralization at the late stage of magmatic fractionation [32,33,45,106].

4.4. Whole-Rock Geochemistry of Mayo Salah Pluton (MSP)

4.4.1. Major Element Characteristics

The major and trace elements composition of samples from MSP are listed in Table 2. On a total alkali versus silica (TAS) diagram [107], all of the samples plot in the granite field. They belong to the sub-alkaline domain [108], to the exception of two samples of pegmatites (Figure 9a).

One sample of MsG has been analyzed and is characterized by (i) a high silica and alkali contents with SiO_2 up to 72.10 wt % and $Na_2O + K_2O$ up to 8.11 wt % respectively; (ii) a moderate content of Al_2O_3 at 13.95 wt %; and (iii) low contents of CaO, Fe_2O_3, P_2O_5, and MgO at 1.75 wt %, 1.62 wt %, 0.06 wt %, and 0.40 wt %, respectively.

The Ms-leucogranite subgroup displays (i) a high silica content, with SiO_2 values ranging from 74.02 to 79.39 wt % in MsLC facies, 73.03 to 75.24 wt % in MsLCm facies, 73.11 to 75.15 wt % in MsLF facies and 70.25 to 73.60 wt % in pegmatites; (ii) a high alkali content in all facies, with $Na_2O + K_2O$ ranging from 6.33 to 9.57 wt % and the higher values in pegmatites up to 12.01 wt %; and (iii) a moderate Al_2O_3 wt % content (12.47–16.11 wt %) with high content in pegmatite up to 16.11 wt %; (iv) a low Fe_2O_3, CaO wt % content in all MsL subtypes, with values ranging from 0.24 to 0.89 wt % and from 0.37 to 1.35 wt %, respectively. Most of the investigated MsL samples have MgO content that is below detection limit but when measurable these contents are up to 0.03 wt %, and they all have lower P_2O_5 below the limit of detection (Table 2). The ASI shows that the MsL subtype is slightly

peraluminous with values of A/CNK ranging from 1.01 to 1.21, whereas MsG is slightly metaluminous with A/CNK = 0.98 ([109]; Figure 9b).

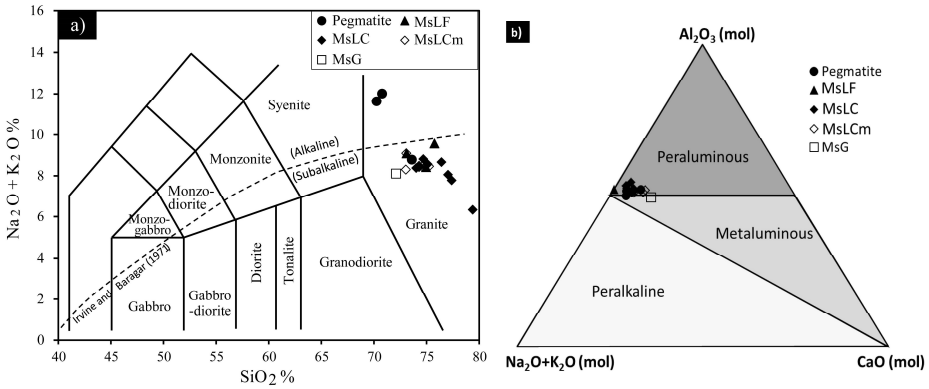

Figure 9. (**a**) Classification of the Mayo Salah granites in the total alkali versus silica (TAS) diagram (SiO_2 vs. Na_2O + K_2O) petrological subdivisions from [107]; alkaline-subalkaline boundary line from [108]; (**b**) classification diagram of Shand [109] showing the peraluminous character of Mayo Salah pluton.

The A vs. B diagram [A = Al − (Na + K + 2Ca), B = Fe + Mg + Ti] of Debon and Lefort [110] shows that all of the MsL samples are peraluminous, with the A parameter ranging from 1.86 to 41.81 and the B parameter ranging from 1.14 to 11.41 (Table 2). In this diagram (Figure 10) the MsL have a positive A parameter and a mafic mineral content (B parameter) that is below 10%, and a peraluminosity index that substantially increases during fractionation [111]. The MsL subgroup plots in the field of anatectic granitoids of the crustal peraluminous domain [111], they show the trend of muscovite ± topaz granite or L-type granites like leucogranite of Beauvoir and St Sylvestre in the French Massif Central [112]. The MsG is metaluminous with a negative A parameter of −5.07 and a B parameter of 33.24, and plots in the field of mantle metaluminous to peraluminous domain.

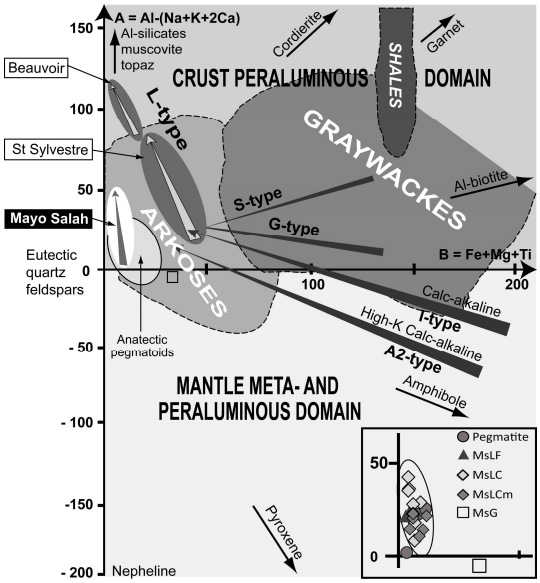

Figure 10. Plot of the Mayo Salah samples (detailed in inset) in the classification diagram Peraluminous index (A = Al − [Na + K + 2Ca]) versus differentiation index (B = Fe + Mg + Ti) of [110]. The trends of major rock-forming minerals are plotted. They are dominantly peraluminous. Graywacke and arkose may be metaluminous if they have carbonate cement. Modified after [111].

Table 2. Major (wt %) and trace (ppm) element compositions of the various facies of the Mayo Salah pluton.

Rock Types	**Ms-Leucogranite (MsL)**																			**Ms-Granite**
Facies	**Pegmatite**			**MsLF**			**MsLC**								**MsLCm**					**MsG**
Sample	**MS37**	**MS27**	**MS37a**	**MS21**	**MS25a**	**MS36a**	**MS34**	**MS35a**	**MS35b**	**MS35C**	**MS39**	**MS40**	**MS41**	**MS45**	**MS28b**	**MS28c**	**MS30**	**MS31**	**MS33a**	**MS38**	**MS44**
SiO_2	70.25	73.60	70.78	73.11	74.96	75.75	75.11	79.39	77.04	77.39	74.69	74.02	74.29	76.42	74.60	73.03	74.29	75.24	73.08	74.29	72.10
TiO_2	b.d.	b.d.	b.d.	0.03	b.d.	b.d.	0.03	b.d.	b.d.	b.d.	0.02	b.d.	0.02	0.02	0.03	0.04	b.d.	0.04	b.d.	0.02	0.24
Al_2O_3	16.11	14.51	15.64	15.33	14.44	12.47	14.25	12.48	14.02	13.66	14.32	14.56	14.35	13.99	14.52	14.71	14.18	13.65	15.28	14.35	13.95
Fe_2O_3t	0.64	0.89	0.26	0.44	0.41	0.24	0.64	0.32	0.34	0.32	0.51	0.48	0.42	0.47	0.77	0.88	0.47	0.64	0.37	0.42	1.62
MnO	0.16	0.06	0.10	0.12	0.16	0.04	0.07	0.08	0.11	0.14	0.08	0.16	0.09	0.06	0.13	0.13	0.09	0.09	0.17	0.09	0.04
MgO	b.d.	b.d.	b.d.	0.02	b.d.	b.d.	0.03	b.d.	b.d.	b.d.	b.d.	b.d.	0.02	0.02	b.d.	b.d.	b.d.	b.d.	b.d.	0.02	0.40
CaO	0.60	1.09	0.73	0.80	0.72	b.d.	0.48	0.42	0.37	0.39	0.65	0.78	0.83	0.77	1.30	1.35	0.85	0.88	0.87	0.83	1.75
Na_2O	2.26	3.06	2.12	4.91	4.82	1.78	4.71	4.86	4.97	4.90	4.77	4.72	4.57	4.94	4.03	3.87	4.29	4.17	5.54	4.57	3.96
K_2O	9.37	5.73	9.89	4.18	3.60	7.79	3.86	1.47	3.08	2.87	4.05	3.66	3.86	3.72	4.43	4.43	4.19	4.30	3.56	3.86	4.15
P_2O_5	b.d.	b.d.	b.d.	b.d.	b.d.	b.d.	b.d.	b.d.	b.d.	b.d.	b.d.	b.d.	b.d.	b.d.	b.d.	b.d.	b.d.	b.d.	b.d.	b.d.	0.06
LOI	0.92	1.26	0.74	0.87	1.04	0.43	0.94	0.88	0.88	0.82	0.81	1.35	1.16	0.58	1.45	1.45	1.06	1.15	1.02	1.16	1.69
Total	100.31	100.19	100.26	99.81	100.14	98.50	100.10	99.89	100.81	100.49	99.89	99.72	99.61	100.98	101.25	99.88	99.43	100.16	99.89	99.61	99.95
Ba	84	24	38	11	2.1	3.0	145	11	5.6	31	30	18	14	14	21	20	17	11	58	25	452
Be	2	2	1	4	6	3	10	4	4	4	6	4	4	9	7	6	5	4	6	6	6
Bi	2	0.20	1.5	0.50	5.4	0.76	0.75	8.4	7.2	3.4	0.92	2.1	0.29	0.13	0.94	0.97	5.8	0.35	1.3	1.2	0.46
Cs	5.8	3.3	5.2	8.9	11	6.3	7.4	2.2	4.8	4.5	5.8	9.7	5.9	18	8.8	9.1	2.3	3.9	3.6	3.5	7.7
Cu	19	b.d.	b.d.	b.d.	b.d.	15	b.d.	b.d.	b.d.	b.d.	11	b.d.	b.d.	b.d.	5.7	17	b.d.	b.d.	6.5	b.d.	6.0
Ga	46	48	36	47	48	35	31	45	50	48	36	47	41	32	48	50	40	34	35	44	24
Ge	3.8	4.0	3.7	3.7	4.3	4.9	3.0	4.0	4.4	4.2	3.5	4.3	4.0	3.2	3.4	3.5	3.1	3.0	3.4	3.8	2.1
Hf	1.3	3.0	0.68	8.1	2.9	4.1	4.2	5.2	5.5	5.5	3.7	4.4	6.5	2.6	6.9	7.4	4.3	4.9	5.8	6.6	5.0
Nb	38	49	16	94	88	50	72	89	81	79	52	63	74	40	79	82	54	71	79	40	23
Pb	92	56	95	44	44	81	54	25	33	31	56	50	37	49	50	48	48	53	55	50	25
Rb	1415	868	1367	896	892	1182	509	333	792	732	635	844	867	567	810	835	573	552	543	623	263
Sc	4.9	11	2.2	4.4	2.8	1.3	3.0	b.d.	b.d.	b.d.	4.0	6.8	5.1	4.1	28	29	11	4.2	7.7	5.1	3.3
Sn	79	145	34	85	55	148	28	46	71	62	105	70	72	77	143	161	83	53	43	52	7.6
Sr	12	14	11	12	3.8	4.9	47	24	6.6	8.1	12	5.8	13	19	11	10	11	15	17	13	188
Ta	9.0	17	3.5	49	18	35	18	33	30	32	8.7	16	31	11	13	13	6.8	7.8	13	13	3.9
Th	3.3	8.4	2.1	19	11	6.6	22	13	11	13	15	25	16	28	19	21	13	22	23	27	26
U	7.6	5.1	3.3	24	5.7	3.1	16	6.5	4.5	4.7	12	15	13	12	21	22	11	16	24	16	7.6
V	0.94	0.84	1.6	0.95	0.74	b.d.	2.3	b.d.	b.d.	b.d.	b.d.	b.d.	b.d.	0.74	b.d.	0.74	0.81	2.3	1.1	b.d.	13
W	2.4	4.0	2.4	3.3	1.4	0.91	1.1	2.0	1.7	1.6	1.1	1.5	2.9	0.7	2.2	2.3	6.4	4.0	2.4	2.1	28
Y	71	57	65	48	72	9.6	97	17	18	17	157	77	44	32	220	221	115	90	123	172	21
Zn	135	145	78	83	171	76	51	107	165	174	77	160	58	58	159	178	98	57	72	77	62

Table 2. *Cont.*

Rock Types	Ms-Leucogranite (MsL)																				Ms-Granite
Facies	Pegmatite			MsLF			MsLC								MsLCm						MsG
Sample	MS37	MS27	MS37a	MS21	MS25a	MS36a	MS34	MS35a	MS35b	MS35C	MS39	MS40	MS41	MS45	MS28b	MS28c	MS30	MS31	MS33a	MS38	MS44
Zr	10	22	5.6	57	19	20	58	29	30	30	38	35	48	28	73	79	46	54	57	61	132
La	13	3.7	11	5.5	6.2	2.8	9.2	13	10.0	10	5.7	11	3.5	2.9	4.4	6.0	3.6	2.5	4.8	2.8	37
Ce	21	7.3	15	12	11	4.3	18	28	23	27	7.0	14	10	6.8	11	16	8.6	5.6	5.9	7.3	69
Pr	4.3	1.3	3.8	1.9	2.4	0.68	2.4	5.0	3.7	3.8	1.7	3.8	1.1	0.95	1.8	2.5	1.4	0.82	1.3	1.1	7.7
Nd	19	5.8	17	7.1	11	2.7	9.8	19	14	14	8.4	16	3.8	3.8	9.2	12	6.6	3.8	6.3	5.9	26
Sm	8.8	2.7	8.2	3.1	6.3	1.1	4.3	8.0	5.7	5.6	5.0	5.7	1.7	1.7	5.7	6.8	3.8	2.7	4.3	3.9	4.7
Eu	0.26	0.09	0.21	0.12	0.12	0.07	0.24	0.04	0.04	0.05	0.44	0.33	0.08	0.13	0.13	0.14	0.10	0.13	0.42	0.11	0.68
Gd	9.1	2.9	8.4	3.3	8.4	1.2	6.1	6.0	4.6	4.3	10	5.9	2.1	2.2	9.8	11	5.8	5.1	9.2	6.4	3.7
Tb	1.7	0.63	1.6	0.77	1.8	0.27	1.4	1.0	0.91	0.84	2.4	1.2	0.61	0.55	2.1	2.2	1.3	1.3	2.3	1.5	0.60
Dy	9.4	4.3	8.2	5.5	9.9	1.7	10	4.5	4.5	4.2	17	8.3	4.7	4.0	14	15	8.7	9.9	17	11	3.6
Ho	1.4	0.86	1.3	1.2	1.6	0.30	2.2	0.49	0.54	0.49	3.6	1.7	1.1	0.88	2.9	3.0	1.8	2.3	3.7	2.5	0.71
Er	3.1	2.4	2.7	3.6	3.3	0.73	6.3	0.80	0.90	0.86	9.2	4.8	3.5	2.4	7.5	7.8	4.9	6.4	9.3	7.7	1.9
Tm	0.44	0.40	0.38	0.64	0.47	0.12	1.1	0.09	0.10	0.10	1.4	0.87	0.64	0.40	1.1	1.2	0.81	1.1	1.4	1.4	0.30
Yb	2.9	2.9	2.4	5.0	3.0	0.75	8.1	0.45	0.52	0.49	9.0	6.7	5.1	2.9	7.6	7.9	5.8	7.6	9.3	11	2.2
Lu	0.35	0.40	0.29	0.76	0.35	0.09	1.2	0.05	0.05	0.05	1.3	0.94	0.78	0.42	1.1	1.1	0.84	1.1	1.3	1.6	0.32
NK	11.63	8.79	12.01	9.09	8.42	9.57	8.57	6.33	8.06	7.78	8.82	8.38	8.43	8.67	8.46	8.30	8.48	8.46	9.09	8.43	8.11
A*	22.12	24.93	1.86	24.41	25.28	21.33	28.43	41.81	35.67	34.70	17.56	27.43	22.40	8.18	13.87	21.28	20.06	10.54	14.25	22.40	-5.07
B*	7.98	11.11	3.30	6.42	5.09	2.94	9.01	3.97	4.26	3.97	6.62	5.96	5.96	6.58	10.04	11.41	5.93	8.51	4.58	5.96	33.24
A/CNK	1.08	1.10	1.01	1.09	1.10	1.10	1.11	1.21	1.15	1.15	1.07	1.11	1.09	1.03	1.05	1.08	1.08	1.04	1.05	1.09	0.98
Nb/Ta	4.2	2.9	4.5	1.9	5.0	1.4	4.0	2.7	2.7	2.5	6.0	3.9	2.4	3.7	5.9	6.1	8.0	9.0	6.1	3.1	5.8
Zr/Hf	8.0	7.5	8.2	7.1	6.8	4.8	14	5.6	5.5	5.4	10	8.1	7.3	10	11	11	11	11	9.8	9.2	27
K/Rb	55	55	60	39	33	55	63	37	32	33	53	36	37	54	45	44	61	65	54	51	131
Σ REE	95	36	81	51	66	17	80	86	69	72	82	82	39	30	79	92	54	50	76	64	158
Σ LREE	66	21	56	30	37	12	44	73	57	61	28	51	21	16	33	44	24	16	23	21	145
Σ HREE	28	15	25	21	29	5	36	13	12	11	54	30	19	14	46	49	30	35	53	43	13
$(La/Yb)_N$	3.1	0.91	3.3	0.79	1.5	2.7	0.82	20	14	15	0.45	1.2	0.50	0.71	0.42	0.54	0.44	0.23	0.37	0.19	12
$(La/Sm)_N$	0.92	0.90	0.87	1.1	0.63	1.6	1.4	1.0	1.1	1.2	0.73	1.3	1.3	1.1	0.50	0.57	0.60	0.59	0.71	0.47	5.0
$(Gd/Yb)_N$	2.6	0.82	2.9	0.56	2.3	1.3	0.63	11	7.3	7.2	0.96	0.72	0.35	0.62	1.1	1.1	0.82	0.55	0.82	0.48	1.4
Eu/Eu*	0.09	0.10	0.08	0.11	0.05	0.18	0.14	0.02	0.03	0.03	0.18	0.17	0.13	0.20	0.05	0.05	0.07	0.11	0.20	0.07	0.49

b.d. = below detection limit; A* = [Al − (Na + K + 2Ca)], B* = (Fe + Mg + Ti); A/CNK = $Al_2O_3/CaO + Na_2O + K_2O$ (mol); NK =$Na_2O + K_2O$ (mol).

4.4.2. Trace Element and REE Patterns

The chondrite-normalized REE [113] patterns and the upper continental crust-normalized incompatible element patterns [114] of representative samples of the MSP are presented in Table 2 and in Figure 11a,b.

The Nb-Ta barren granite MsG is the most enriched in REE (158 ppm). Its chondrite-normalized REE pattern (Figure 11a) is moderately fractionated with $(La/Yb)_N$ = 12, and it shows an Eu negative anomalies (Eu/Eu* = 0.49) and a flat HREE profile (Gd_N/Yb_N = 1.4), as well as a pronounced fractionation within the LREE with $(La/Sm)_N$ = 5.0 when compared to the flat HREE. In the spider diagram, the MsG expresses homogenous composition with negative anomalies in Zr, Sr and Eu (Figure 11b), and positive U and Ta anomalies.

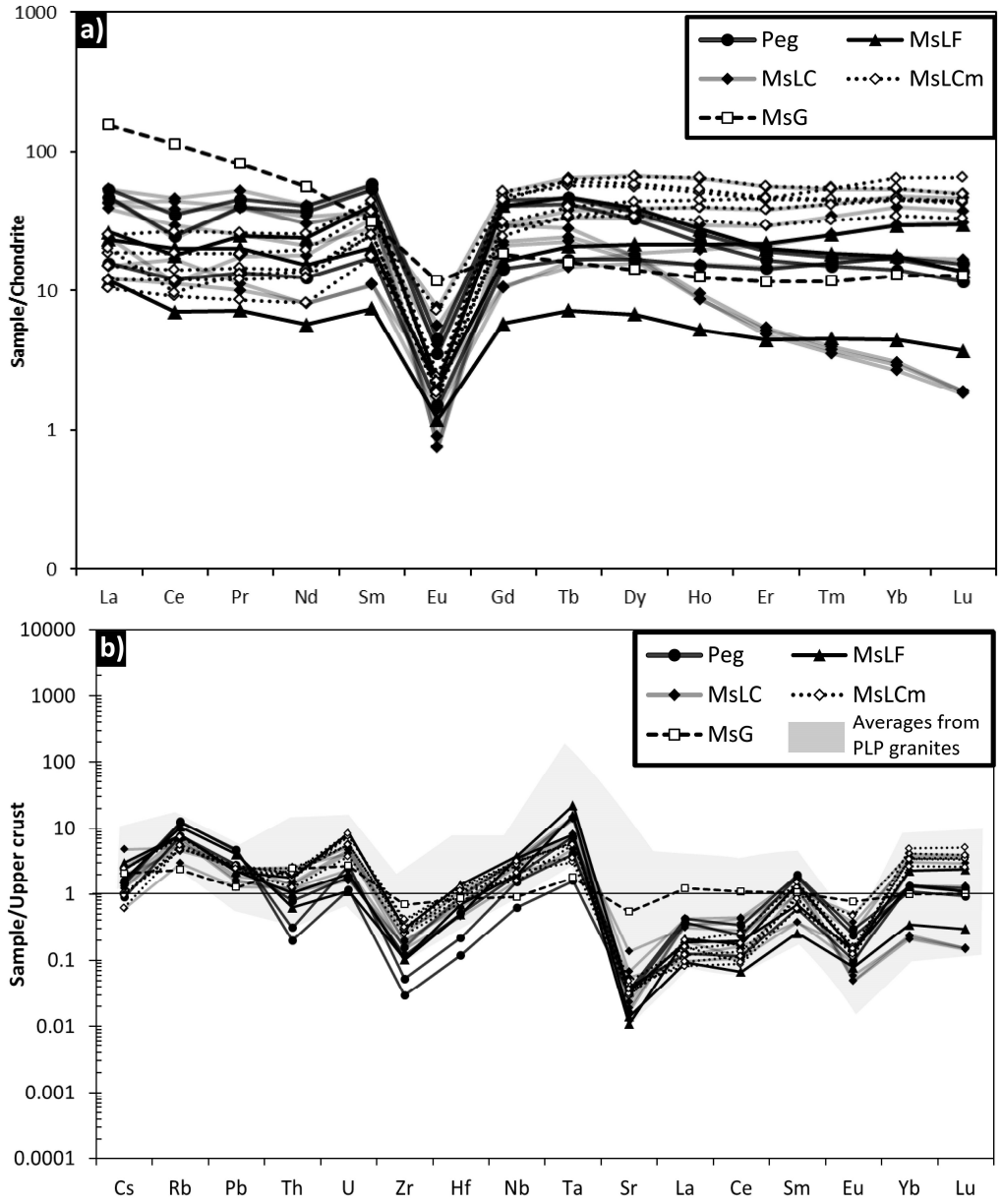

Figure 11. (**a**) Chondrite-normalized REE patterns for the MsL and MsG whole-rocks of the Mayo Salah pluton. Normalization after [113]; and, (**b**) Upper crust-normalized incompatible element patterns for the Mayo Salah pluton. Normalization after [114]. Averages of distribution of rare-elements in peraluminous low phosphorous (PLP) granites are from [4].

The abundance of REE in the MsL group is low and displays variation ranging from 17 to 95 ppm. In the chondrite-normalized REE patterns (to the exception of three samples of the MsLC subgroup: MS35a, MS35b, MS35c, see below), the MsL display flat patterns and exhibit slight to none fractionation for all the subgroup of MsL with $(La/Yb)_N$ = 0.193.1 (Figure 11a). They also exhibit a lower fractionation within the LREE ($(La/Sm)_N$ = 0.47–1.6) than within the HREE ($(Gd/Yb)_N$ = 0.35–2.9). Granites of the MsL subgroup are characterized by a strong negative Eu anomaly (Eu/Eu* = 0.05–0.20), which is typical of leucogranite rocks that expressed significant plagioclase fractionation. In the pegmatite facies, the chondrite-normalized REE patterns are slightly fractionated ($(La/Yb)_N$ = 0.91–3.3) and they show clear Eu negative anomalies (Eu/Eu* = 0.08–0.10). The HREE are depleted and display weakly fractionated patterns (Gd_N/Yb_N = 0.82–2.9). Two main subtypes of the MsL have a singular behavior. (i) The MsLC granites have REE contents from 30 to 86 ppm with a flat REE pattern $(La/Yb)_N$ = 0.45–1.2; to the exception of three samples (MS35a, MS35b, MS35c), which appear to be moderately fractionated with $(La/Yb)_N$ = 20, 14 and 15, respectively. These three samples display strong Eu negative anomalies (Eu/Eu* = 0.02, 0.03, 0.03), and significant depletions in HREE $(Gd/Yb)_N$ = 11, 7.3, 7.2, respectively, probably due to the abundance of monazite and garnet in this facies; (ii) The MsLCm granites are characterized by low ∑REE contents (50–92 ppm), with a low fractionation of the LREE over the HREE ($(La/Sm)_N$ from 0.47 to 0.71, $(La/Yb)_N$ from 0.19 to 0.54, and $(Gd/Yb)_N$ from 0.48 to 1.1; Figure 11a), as marked by the flat REE patterns. In the trace elements spider diagram (Figure 11b), the MsL samples display a positive slope for Rb, U, and Nb elements, and a negative slope of Zr, Sr, and Eu elements. This distribution of trace elements is characteristic of metaluminous to peraluminous low phosphorous (PLP) rare-element granites [4]. A high degree of magmatic fractionation in MsL is reflected by the low K/Rb value (32–65).

4.4.3. Trace Element Features

The Nb content in all of the samples of the MSP ranges from 16 to 94 ppm, and increases from the MsG to tbe MsL subgroup. (i) The MsG displays the lowest Nb concentration at 23 ppm; (ii) the pegmatites have values between 16 and 38 ppm; (iii) the MsLCm and the MsLC have Nb contents ranging from 40 to 82 ppm and from 40 to 89 ppm, respectively; and, (iv) MsLF have values ranging from 50 to 94 ppm (Table 2).

The Ta is less concentrated than Nb (from 3.5 to 49 ppm), but it displays the same distribution than Nb in the different facies of the MSP. The Ta content is of 3.9 ppm in the MsG, from 3.5 to 17 ppm in pegmatites, from 6.8 to 13 ppm in the MsLCm, from 8.7 to 33 ppm in the MsLC, and from 18 to 49 ppm in the MsLF.

The Sn content displays values ranging from 43 to 161 ppm in all of the facies to the exception of (i) the MsG where the Sn content is down to 7.6 ppm, and of (ii) the MsLC with moderate contents from 28 to 105 ppm (Table 2).

According to Ballouard et al. [22], the Nb/Ta ratios can be used as a geochemical indicator to discriminate barren granites (Nb/Ta > 5) from rare-metal granites (Nb/Ta < 5). In samples from the MSP, the Nb/Ta ratio varies from 1.4 to 9.0 (Figure 12a) and samples with a low Nb/Ta ratio displays the highest content of Nb and Ta. Thus MsLC and MsLF have Nb/Ta < 5, and are mineralized, whereas the MsLCm and the MsG have Nb/Ta > 5 and are barren. This geochemical discrimination is also observed using the Zr/Hf ratio that is typically low in RMG (<18) [22]. The Zr/Hf ratio in all leucogranite subtypes MsLC (5.4–14), MsLF (4.8–7.1), and MsLCm (9.2–11) indicates that these granites are in the field of RMG, while the MsG (Zr/Hf = 27) is barren (Figure 12b and Table 2).

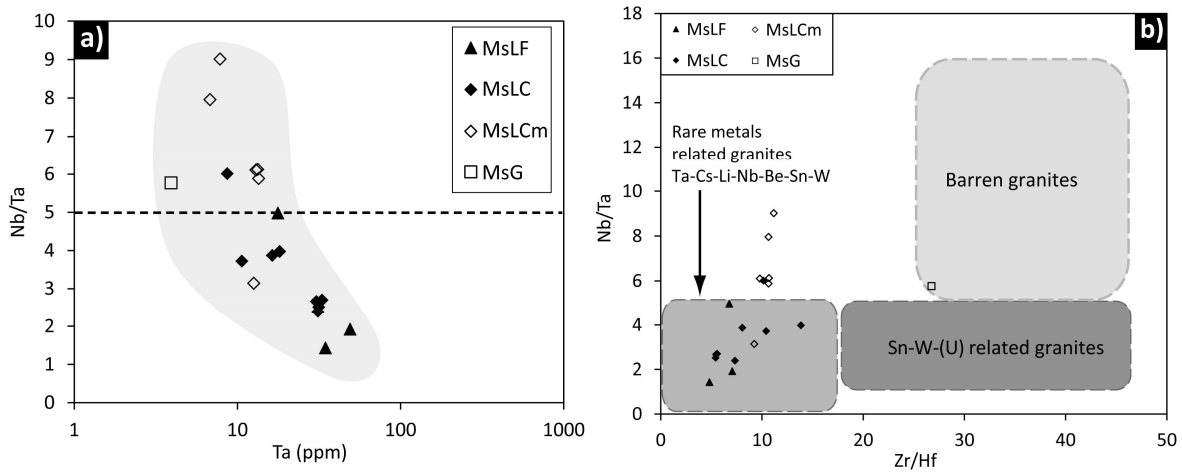

Figure 12. (**a**) Nb/Ta versus Ta (ppm) diagram of the Mayo Salah granitic facies showing the evolution of peraluminous granites during fractionation [22]; and, (**b**) Nb/Ta versus Zr/Hf diagram allowing for the comparison of the granitic rock samples of Mayo Salah to typical geochemical domains of rare-metals related granites (Ta-Cs-Li-Nb-Be-Sn-W), Sn-W-(U) related granites and barren granites, after [22]. Note that the MsG and is barren.

4.5. U-Pb Dating of Columbite and Monazite

Geochronological constraints on the different facies of the Mayo Salah granites were obtained on several grains of coltan (columbite-Mn) and monazite that were separated from the coarse-grained muscovite leucogranite (Table 1) that corresponds to the main mineralized facies of the MSP (Figure 3). Among the three selected samples, 14 columbite and nine monazite crystals were individually analyzed in sample MS35c (MsLC facies), and 10 columbite-Mn crystals and one monazite crystal in sample MS38 (MsLCm facies). A maximum of 38 representative spots from the columbite crystals (Table 3) and 23 spots from the monazite crystals (Table 4) were defined using BSE images (Figures 13a and 14a).

Table 3. U-Pb columbite dating using Laser Ablation-Inductively Coupled Plasma-Mass Spectrometry (LA-ICP-MS) from the MsLC facies (sample MS35c) and MsLCm facies (sample MS38) of the Mayo Salah Pluton. Errors are listed at 1 sigma.

Sample	Spot Number	Concentrations (ppm)				Isotope Ratios				Ages (Ma)	
		Pb	U	Th	Th/U	$^{207}Pb/^{206}Pb$	Err (%)	$^{238}U/^{206}Pb$	Err (%)	$^{206}Pb/^{238}U$	Err (Abs.)
MS35c	1	603	6537	310	0.05	0.0596	1.02	10.057	1.17	611	7
	2	374	4046	270	0.07	0.0629	1.03	10.209	1.16	602	7
	3	419	4610	198	0.04	0.0592	1.03	10.195	1.16	603	7
	4	195	2118	92	0.04	0.0604	1.04	10.108	1.16	608	7
	5	538	2725	455	0.17	0.2169	1.03	7.394	1.17	818	9
	6	84	1208	74	0.06	0.0684	1.07	13.868	1.16	449	5
	7	458	3516	280	0.08	0.1637	1.03	10.121	1.16	607	7
	8	275	2904	164	0.06	0.0682	1.04	10.141	1.17	606	7
	9	340	3684	170	0.05	0.0587	1.04	10.052	1.17	611	7
	10	398	4675	218	0.05	0.0913	1.04	12.277	1.17	505	6
	11	333	3600	180	0.05	0.0589	1.05	10.058	1.17	611	7
	12	345	3741	233	0.06	0.0586	1.04	10.099	1.16	609	7
	13	299	3452	188	0.05	0.0629	1.05	10.909	1.17	565	6
	14	300	3304	150	0.05	0.0587	1.06	10.217	1.16	602	7
	15	327	3578	165	0.05	0.0587	1.07	10.168	1.17	605	7
	16	293	3528	146	0.04	0.0634	1.07	11.378	1.16	543	6
	17	772	5098	583	0.11	0.1918	1.06	9.117	1.17	671	7
	18	253	2646	219	0.08	0.0649	1.06	10.045	1.17	612	7
	19	190	1743	94	0.05	0.0809	1.08	9.200	1.17	665	7
	20	181	1996	92	0.05	0.0599	1.08	10.253	1.17	600	7
	21	328	3591	184	0.05	0.0585	1.09	10.172	1.17	605	7
	22	189	2059	87	0.04	0.0613	1.09	10.206	1.16	603	7
	23	206	2273	80	0.04	0.0607	1.10	10.280	1.16	599	7

Table 3. *Cont.*

Sample	Spot Number	Concentrations (ppm)				Isotope Ratios				Ages (Ma)	
		Pb	U	Th	Th/U	$^{207}Pb/^{206}Pb$	Err (%)	$^{238}U/^{206}Pb$	Err (%)	$^{206}Pb/^{238}U$	Err (Abs.)
MS38	24	7228	175722	4077	0.02	0.1179	1.09	29.104	1.19	218	3
	25	188	2121	95	0.04	0.0602	1.13	10.466	1.19	588	7
	26	7050	95173	27522	0.29	0.4241	1.11	29.985	1.20	212	2
	27	386	4299	318	0.07	0.0592	1.13	10.459	1.19	589	7
	28	403	4452	343	0.08	0.0607	1.15	10.480	1.18	588	7
	29	478	5295	376	0.07	0.0580	1.15	10.413	1.19	591	7
	30	466	5096	377	0.07	0.0580	1.19	10.321	1.18	596	7
	31	377	4162	295	0.07	0.0583	1.20	10.458	1.18	589	7
	32	706	6215	542	0.09	0.1484	1.30	11.361	1.17	544	6
	33	294	3190	193	0.06	0.0599	1.34	10.516	1.17	586	7

Table 4. U-Pb monazite dating using LA-ICP-MS from the MsLC facies (sample MS35c) and MsLCm facies (sample MS38) of the Mayo Salah Pluton.

Sample	Spot Number	Concentrations (ppm)				Isotope Ratios				Ages (Ma)	
		Pb	U	Th	Th/U	$^{206}Pb/^{238}U$	Err (1σ)	$^{207}Pb/^{235}U$	Err (1σ)	$^{206}Pb/^{238}U$	Err (1σ)
MS35c	1	2240	2732	72,814	26.7	0.0969	0.001	0.859	0.011	596	8
	2	1093	582	47,738	82.1	0.2374	0.003	12.519	0.162	1372	16
	3	923	542	32,103	59.2	0.0990	0.001	0.794	0.012	608	8
	4	1085	738	37,913	51.4	0.1572	0.002	6.395	0.083	941	12
	5	912	453	31,492	69.6	0.0977	0.001	0.788	0.012	600	8
	6	959	309	39,680	128.5	0.1942	0.003	9.273	0.126	1144	14
	7	1377	1632	58,942	36.1	0.1649	0.002	6.995	0.091	983	12
	8	1112	775	44,679	57.7	0.1687	0.002	7.300	0.097	1004.	12
	9	1921	2716	74,383	27.4	0.1100	0.001	2.272	0.030	6726	8
	10	1786	1750	81,966	46.8	0.1525	0.002	6.049	0.080	914	11
	11	3711	5897	116,034	19.7	0.0984	0.001	1.036	0.014	605	8
	12	3665	5875	108,799	18.5	0.0959	0.001	0.947	0.013	590	7
MS38	13	1965	2600	61,206	23.5	0.0956	0.001	0.777	0.011	588	7
	14	2453	4132	73,798	17.9	0.0954	0.001	0.757	0.010	587	7
	15	1612	1988	53,603	27.0	0.0977	0.001	0.842	0.012	600	8
	16	2344	2871	80,714	28.1	0.0965	0.001	1.181	0.016	594	7
	17	1758	815	71,159	87.3	0.0992	0.001	1.522	0.032	609	8
	18	817	182	28,466	156.4	0.1519	0.002	6.483	0.099	911	12

4.5.1. The Coarse-Grained Muscovite Leucogranite (MsLC, Sample MS35c)

Sample MS35c is characterized by coarse grained quartz, feldspar, muscovite, and minor fluorite, garnet, monazite, zircon, and oxide minerals, such as cassiterite and wolframite (Table 1). Late stage microfractures or veinlets filled with quartz are also locally observed. This rock was collected at the northern part of the pluton, 200 m from the national road (Figure 3).

The columbite grains extracted from this rock are dominated by a homogenous population of dark, euhedral crystals. No inherited cores were observed in the population. Crystals range in size from ca. 100 to 350 µm, with the majority being around 150 µm. The BSE imaging shows that the grains are usually fractured and fairly homogeneous with patchy core and little zoning on their outer rim (Figure 13a). Fourteen grains have been analyzed (Table 3). The data plot in a concordant to discordant position in a Tera-Wasserburg Concordia diagram (Figure 13b). The discordant analyses can be best explained by a combination between Pb loss and the presence of initial common Pb. A group of 11 concordant data yield a Concordia date of 603.2 ± 5.3 Ma (MSWD = 1.7; Figure 13b insert).

Monazite grains extracted in the sample MS35c, have a medium size (100 to 250 µm), and range from colorless to pale pink with few cracks. The Th/U ratios are high and range from 18.5 to 69.6 (Table 4). A total of 12 spot analyses on nine grains were obtained for sample MS35c, yielding $^{208}Pb/^{232}Th$ dates ranging from 410.3 to 612.3 Ma. Most of the analyses show the presence of initial common Pb within these monazite grains. Plotted in a Concordia diagram (Figure 13c), they define a lower intercept date of 590 ± 13 Ma (MSWD = 2.4). The two concordant analyses yield a Concordia date of 597.1 ± 7.9 Ma (MSWD = 1.5, Probability = 0.23) (Figure 13c insert).

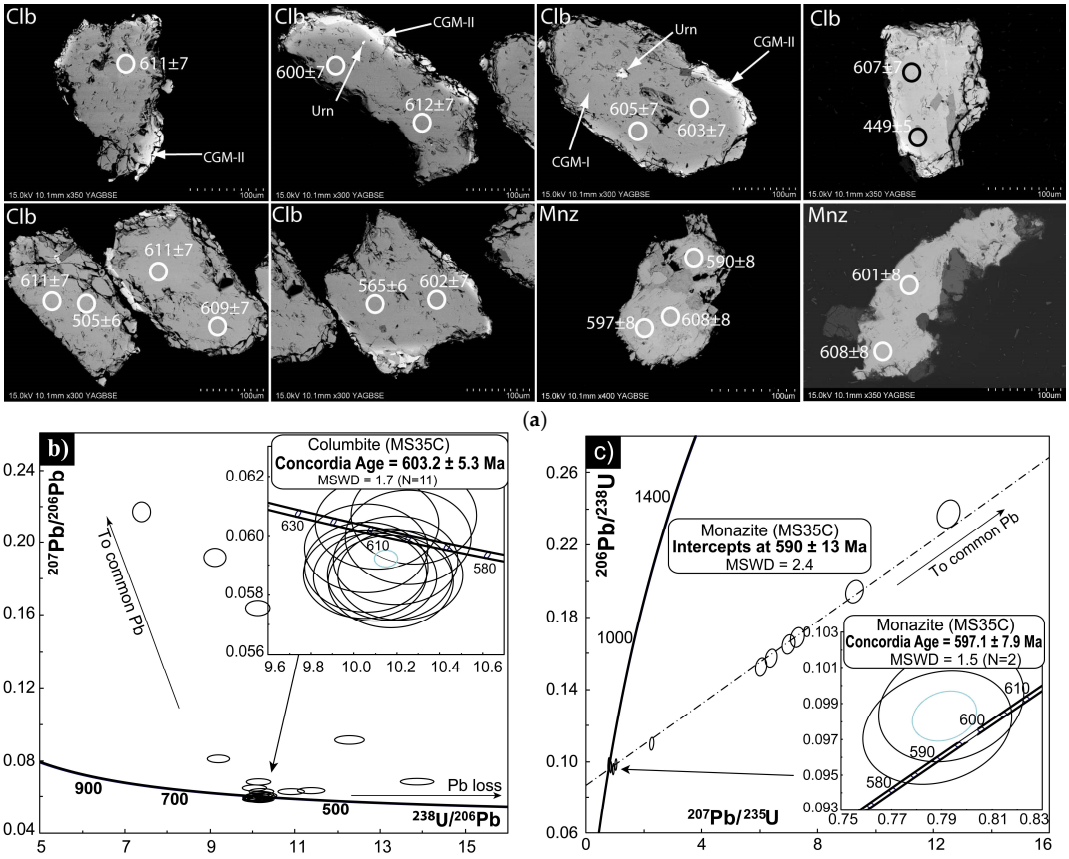

Figure 13. (**a**) BSE image of representative dating columbite (Clb) and monazite (Mnz) of MsLC facies (sample MS35C). The ablation spots' positions are marked with a white circle. Abbreviations: Urn: uraninite, Thr: thorite, CGM-I: primary columbite-group mineral, CGM-II: secondary columbite-group mineral; (**b**) U-Pb Concordia diagram of columbite from MsLC facies of the Mayo Salah pluton; and, (**c**) U-Pb Concordia diagram of monazite from MsLC facies of the Mayo Salah pluton.

4.5.2. The Coarse-Grained Muscovite Leucogranite, Mn-Oxide-Bearing (MsLCm, Sample MS38)

The sample MS38 corresponds to the Mn-oxides bearing coarse-grained muscovite leucogranite (MsLCm). It is the transitional facies between the muscovite granite (MsG) in the south and the main coarse-grained muscovite leucogranite (MsLC) in the north of the Mayo Salah pluton (Figure 3). This sample was collected in the southeastern part of the pluton and it is a medium- to coarse-grained sample with local porphyritic texture that was marked by the Mn-oxide concentrations. The mineralogy consists in albite, K-feldspar (microcline), quartz, muscovite, and Mn-oxides. Accessory minerals are represented by zircon, garnet, monazite, and oxides (rutile, wolframite, cassiterite, coltan, and pyrochlore). Calcite and fluorite are expressed as secondary mineral phases (Table 1).

The columbite grains extracted from this rock are dark and euhedral crystals. BSE images show that the grains are usually fractured and fairly homogeneous with patchy core zoning (Figure 14a). Their size varies from 100 to 200 µm. Some crystals host uraninite and thorite inclusions (Figure 14a). The Th/U ratios range from 0.02 to 0.08 (Table 2), which is in agreement with the magmatic nature of the analyzed columbite grains. With the exception of three analyses that plot in a discordant position (Figure 14b), the remaining seven analyses are concordant and yield a concordia date of 588.3 ± 5 Ma. (MSWD = 1.5, Figure 14b insert).

Only one monazite crystal has been extracted from sample MS38. It presents a medium size (150 µm), is pale pink, with few cracks. The Th/U ratios are high and range from 17.9 to 156.4 (Table 4). A total of six spots were analyzed, yielding $^{208}Pb/^{232}Th$ dates ranging from 519.3 to 634.2 Ma.

The position of the data in the Concordia diagram can be attributed to the presence of a non-negligible amount of initial common Pb in most of this monazite grain. A Concordia date of 581.6 ± 7.2 Ma (MSWD = 1.5) can be calculated with the two concordant data (Figure 14c, insert), while a lower intercept date of 583 ± 19 Ma (MSWD = 3.0) can be calculated using all of the data (Figure 14c).

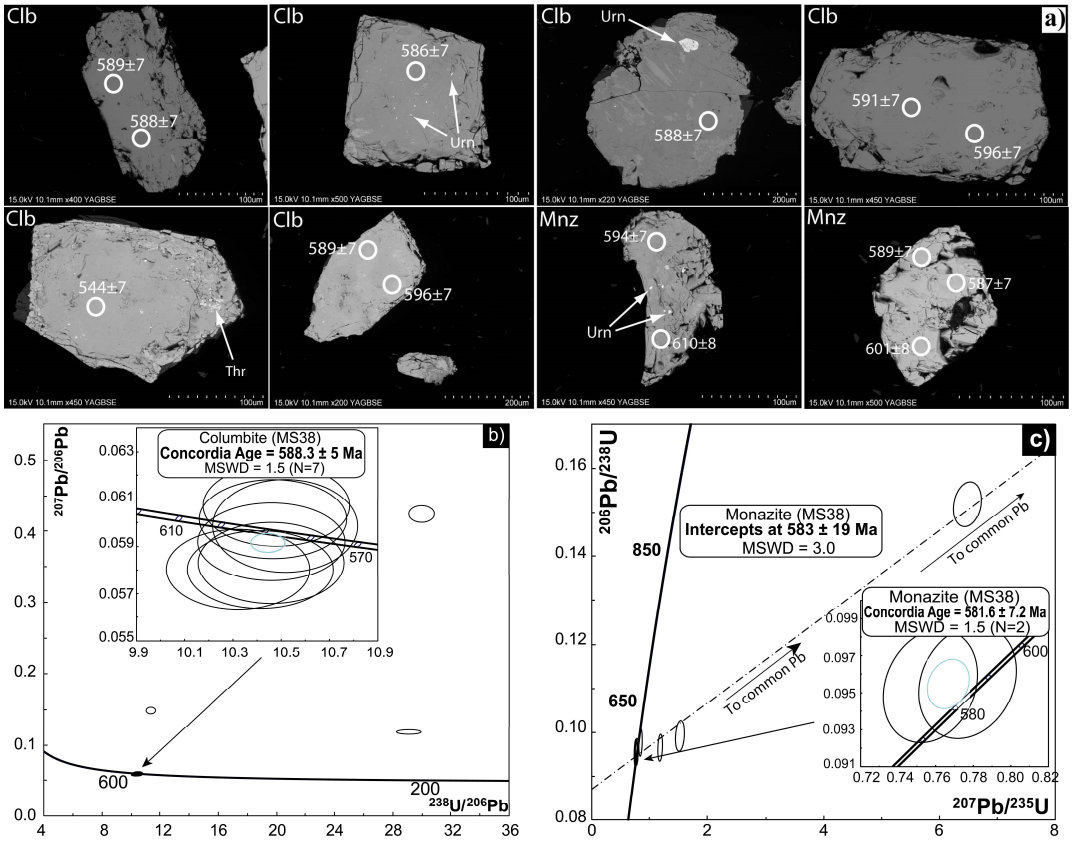

Figure 14. (**a**) BSE image of representative dating columbite (Clb) and monazite (Mnz) of MsLCm facies (sample MS38). The ablation spots' positions are marked with a white circle. Abbreviations: Urn: uraninite, Thr: thorite; (**b**) U-Pb Concordia diagram of columbite from MsLCm facies of the Mayo Salah pluton; and, (**c**) U-Pb Concordia diagram of monazite from MsLCm facies of the Mayo Salah pluton.

5. Discussion

5.1. The Mayo Salah Pluton: A Peraluminous Low-Phosphorous Rare-Metal Granite

The Mayo Salah pluton (MSP) is made of two main rock groups: the metaluminous barren muscovite granite and the mineralized (Nb-Ta-Sn) peraluminous leucogranite (Figure 3; Table 1). It is emplaced as isolated bodies in micaschists and metavolcanics, as described generally for the RMG [4] with example of the Beauvoir granite that is emplaced at shallow levels [6]. The leucogranites of MSP are subalkaline and weakly peraluminous (ASI = 1.01–1.21; Figure 9a,b) with high alkali contents (Na_2O + K_2O from 8.06 to 12.01 wt %). Using the diagram of the peraluminous index versus the differentiation index of Debon and Lefort [110], Cuney [111] discriminated various magmatic fractionation trends among peraluminous, metaluminous, and peralkaline igneous rocks and anatectic pegmatoids (Figure 10). The leucogranite group of the MSP plots in the field of crust peraluminous domain. They have a trend that is comparable to L-type igneous rocks characterized by distinctive increase of ASI during fractionation, and mafic minerals below 10%, and that formed by low degrees of partial melting (<30%) of quartz-feldspar-rich protoliths such as meta-arkose, felsic metavolcanic rocks, or metagranite [115]. Three samples (MS35a, MS35b, MS35c) appear to be

moderately fractionated with $(La/Yb)_N$ of 20, 14 and 15 (Table 2). The latter displays a significant depletion in HREE with $(Gd/Yb)_N$ of 11, 7.3, and 7.2, respectively, which is probably due to abundance of monazite and garnet in this facies [116,117]. They display flat REE patterns $(La/Yb)_N$ = 0.19–3.3 with a strongly negative Eu anomaly (Eu/Eu* = 0.05–0.20) typical of leucogranite [118], and a slight enrichment of HREE in MsLCm subtype (Figure 11a). They have relatively low Zr/Hf (4.8–14) and Nb/Ta (1.4–9.0) ratios that were shown by the positive slope of the Zr-Hf-Nb-Ta profile (Figure 11b). All of these features indicate that the MSP belongs to the peraluminous low-phosphorus (PLP) rare-element granites (Figure 10; [4]), like the topaz granites from Suzhou granite [119], Ahelehedj [120], Cinovec [121,122], Seiffen stock [123], Shizhuyuan, and Chavance [124]. They correspond to the standard class of [16], the highly fractionated I- or A2-type granites of [17], or the magnetite-series granites of [18]. The MsL have a Zr/Hf < 18 and an Nb/Ta < 5, and plot in the field of RMG [22] that was related to Ta-Li-Cs-Nb-Be-Sn-W, while the MsG is barren (Figure 12b). The rare-element mineralization (Nb, Ta, and Sn) of the MSP is expressed as cassiterite and homogeneously disseminated Nb-Ta oxides, such as coltan, rutile, and pyrochlore within the MsL facies (Figures 6 and 7). The Nb-Ta oxides are hosted by the silicate matrix, and display a simple core-rim normal progressive zoning and less frequently an oscillatory zoning (Figure 7). The presence of these oxides as inclusions within most primary minerals, such as muscovite and albite; as well as the inclusion of some albite within the coltan (Figure 6), and chemical zoning of these oxides (Figure 7) allow for interpreting these crystals as magmatic in origin, as described in worldwide studies [4,6,9,10,12,28,36,37,105,125–128]. CGM-I is characterized by high Mn# (0.52–0.89) and low Ta# (0.04–0.19) typical of earlier magmatic-stage products, and the observed differences in Mn# or Ta# values of the primary columbite minerals in the different facies strongly suggest a high differentiated magmatic environment during crystallization of the Mayo Salah leucogranite magma (Figure 8; [12]). The Ta# and Mn# ratios increase from the core to the rim of the crystals, but with small oscillations (Figure 8). The zoning pattern that was observed in the CGM as well as the continuous compositional whole rock geochemistry trends in Ta# and Zr/Hf (Figure 12b) suggest that these geochemical variations are related to magmatic fractionation [28]. Indeed, constant evolution of the Mn# ratio from earlier to late magmatic stage is a typical trend in RMG [4,31] and it is attributed to fractional crystallization in rare-metal-enriched granites and granitic pegmatites [4,9,12]. In the same way, the composition of CGMs from the Mayo Salah leucogranite displays the same features of Ta# variation reported in rare-metal granites worldwide (Figure 15; e.g., [9,12,129]), as well as in granitic pegmatites (e.g., [4,31,128].

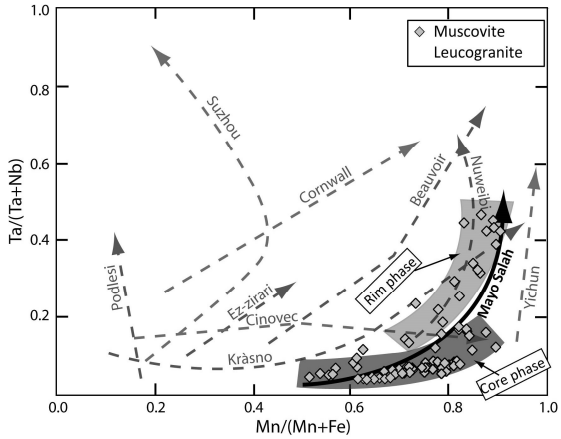

Figure 15. Schematic Ta# vs. Mn# [Ta/(Nb + Ta) vs. Mn/(Mn + Fe)] compositional diagram for columbite-group minerals from the rare-metal granites worldwide. The Mayo Salah pluton (this work); Krásno-Horní Slavkov ore district [12]; Podlesí, Czech Republic [130]; Cínovec, Czech Republic [121]; Cornwall, England ([131]; Ez-zizari, Morocco [132]; Suzhou, China [118]; Nuweibi, Egypt [129]; Beauvoir, France [133]); and, Yichun, China [9,132].

The late stage designated as CGM-II is observed as CGM-I overgrowths as well as veinlets within the primary columbite (Figure 7, Figure 13a, and Figure 16), suggesting a change in the melt composition during the late magmatic stages that were characterized by volatile-rich solutions. In the MsLCm facies, CGM-II is often associated with pyrochlore surrounding CGM-I (Figures 6h and 7o). Pyrochlores are metamict and host inclusions of uraninite and thorite. They present the same features as the other Ta-Nb oxides (TNO) [32,33,45,106]. CGM-II has higher Mn# (0.55–0.90) and Ta# (0.05–0.47) values (Figure 8).

The geochemical and mineralogical features of the Nb-Ta oxide minerals that were described in the MSP express the same trends that have been described by previous experimental studies and natural examples during magmato-hydrothermal processes for Nb-Ta mineralization in peraluminous granite or pegmatite [4,14,15,22,37]: a Nb-rich Mn-columbite earlier stage, observed in the core of minerals, followed by a Ta-rich Mn-columbite later stage. This trend represents changes in the melt composition, with Ta enrichment relative to Nb in the residual melt. Experimental studies show that the lower activity coefficient of Ta in the melt relative to Nb, which is based on the solubility difference of Mn-columbite and Mn-tantalite in subaluminous and peraluminous melts, give an explanation for the progressive enrichment of Ta contents in columbite with increasing fractionation [37]. At the late stage of fractionation, the fractionating melt does not contain a sufficient Ta concentration to precipitate tantalite species of CGM (Figure 8).

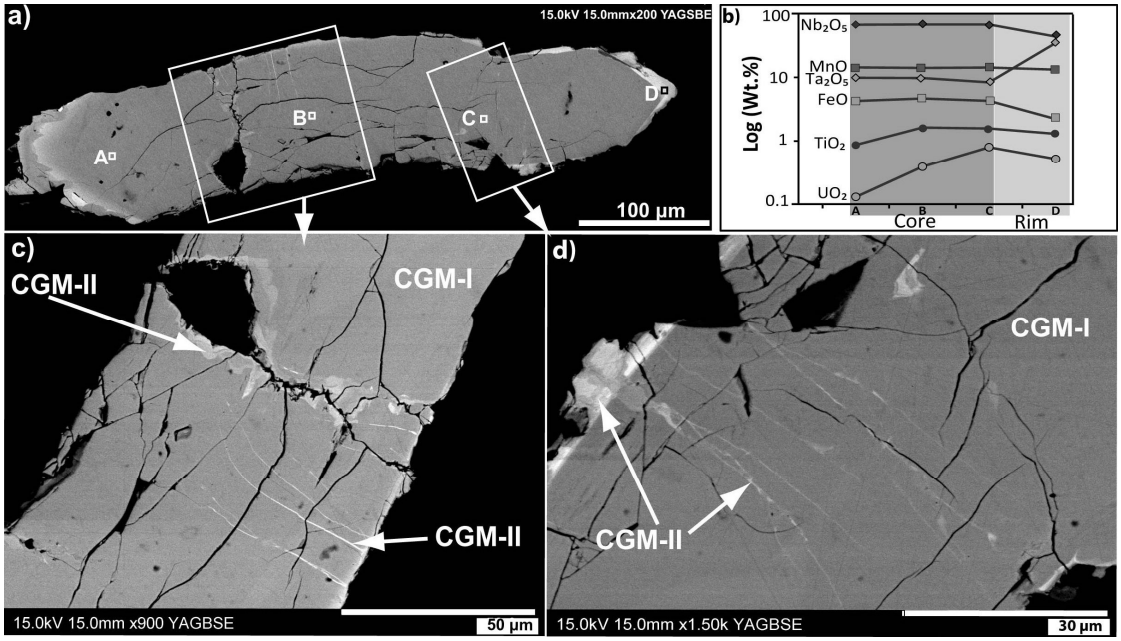

Figure 16. BSE images of CGM-I and CGM-II association in the MsLC facies: (**a**) Simply progressive zoning in a columbite crystal; (**b**) Electron-microprobe profiles across the points A, B, C, D, of the zoned crystal (of Figure 16a), illustrating the variation of Nb, Ta, Mn, Fe, Ti, and U, respectively; (**c**,**d**) Crystal of CGM-I surrounded by CGM-II, which also entered into the CGM-I as a veinlet (arrowed).

5.2. Geotectonic Setting of the Mayo Salah Pluton: Significance in the Northern Cameroon Domain (NCD) of the Central Africa Fold Belt (CAFB)

The Mayo Salah rare-metal bearing low-phosphorous peraluminous granite that was highlighted by this study in the NCD of CAFB in Cameroon rises many questions relative to its geodynamic signification in this area. This type of granite is generally found in the continental collision context [118] and generally represents the evolved term of highly fractionated magma of crustal origin [4].

The MSP occurs as laccolith in volcano-sedimentary schists of Poli group (Figure 3). The pluton presents an E-W elongation in its host schists with concordant contacts. Structural features show

that the deformation decreases progressively from the borders to the weakly deformed core of the pluton, which is typical for composite, multiphase intrusions. In this core, the deformation is expressed as a local mineral lineation (N75E–N110E), underlined by muscovite and quartz (Figure 5h). The microstructure observations indicate that primary muscovite is kinked, plagioclase is sheared, and quartz has undulose extinction (Figure 5n,o). At the northern and southern boundaries of the MSP, the deformation is expressed as a shallow-dipping and as a subvertical foliation stretching or mineral lineation (<12°), respectively. Several faults of NW-SE and E-W direction are identified (Figure 3). The contact between the pluton and its hosts in its northern boundaries is marked by similar fabrics, both within the MsL facies and the schists. Locally, the structures of the host rocks are preserved within xenoliths found in the MsL facies (Figure 5e,f). These elements allow for proposing that this pluton would be related to a E-W and NW-SE fault/shear zone, similar to numerous shear zones and strike-slip faults in the vicinity of this area, like the Tcholliré-Banyo fault at the East [66,69] and the Godé-Gormaya shear zone at the West [68].

The different facies of this pluton underwent numerous fault/fracture and conjugate sinistral/dextral shearing mainly NE-SW (N50E–N70E), E-W (N80–N90E), and WNW-ESE (N110E–N150). The fault and conjugal sinistral/dextral shear zone that was identified in the MSP (Figure 5k–m) are also interpreted as left lateral wrench movements between ca. 613 and 585 Ma and right lateral wrench movements at ca. 585–540 Ma [64,83,134] in the NCD related to the second tectonic event. In the Guider area of NCD, a pluton of syenite dated at 593 ± 4 Ma, is interpreted as late-tectonic during the D_2 event [83]. Indeed, the age of the D_3 is recorded in the different domains of CAFB in Cameroon. Toteu et al. [69] constrained D_3 deformation between ca. 600 and 580 Ma, associated with a post-collisional stage coeval with the development of shear zones, and with the emplacement of late-tectonic calc-alkaline to sub-alkaline granitoids (ca. 600–570 Ma). The age of ca. 601–558 Ma for the D_3 event is also found in Meiganga area of AYD [135]. In the Mayo Salah pluton, the LA-ICP-MS U-Pb dating of coltan (Mn-columbite) and monazite were carried out on two Nb-Ta mineralized MsL facies. The first facies (MsLC) is the most mineralized in Nb-Ta and yields columbite and monazite concordant ages of 603.2 ± 5.3 Ma and 597.1 ± 7.9 Ma, respectively (Figure 13b,c; Table 3). The second facies (MsLCm) is the transitional facies between the mineralized MsL and the barren MsG and yields coltan and monazite concordant ages of 588.3 ± 5 Ma and 581.6 ± 7.2 Ma, respectively (Figure 14b,c; Table 4). These data indicate that the mineralization of Mayo Salah leucogranite is related to a late-Neoproterozoic magmatic event (Pan-African) between ca. 603 and 582 Ma. All of the structural features, when coupled with the ages of this pluton (ca. 603 and 582 Ma), show that the MSP emplaced during late D_2 to syn-D_3 tectonic event recorded in the CAFB.

The tectonic evolution of the CAFB in the northern edge of the Congo Craton is not well defined, but several features, such as (i) arc-type magmatism; (ii) external nappes of regional extent; (iii) granulitic metamorphism; (iv) intensive plutonism that is associated with crustal melting; and, (v) regional strike-slip faults with numerous Pan-African granitoids characterize a long-lived (ca. 800–600 Ma) collisional belt [136]. The late-Neoproterozoic CAFB at the north of the Congo craton was recognized by the widespread occurrence of ca. 600–500 Ma Rb-Sr whole rock and mineral ages [137]. The tectonic evolution of CAFB in the northern edge of the Congo Craton is interpreted as the substantial crustal thickening during the Pan-African clock-wise continent-continent collision at ca. 600 Ma, followed by the exhumation of different crustal levels, the development of regional transcurrent shear zones, and the emplacement of post-collisional granitoids that are younger than ca. 600 Ma [63,72,83,136]. The 603.2 ± 5.3 Ma to 581.6 ± 7.2 Ma U-Pb ages on columbite and monazite of the Mayo Salah rare-element leucogranite, correspond to the ages of late-tectonic granitoids emplaced at ca. 600–580 Ma. These granitoids in the northwest of the Tcholliré-Banyo fault were interpreted as being mainly derived from juvenile crust or crust with lesser degrees of older crustal contamination [68]. The ca. 630–580 Ma ages recorded in zircon grains from syn-tectonic granitoids and on metamorphic rocks [63,66,68,79,93,94], is interpreted as a stage of collision associated with the assembly of west Gondwanaland. This stage ended about ca. 600–580 Ma with a general anatexis that was associated

with southward thrusting of the CAFB onto the Congo craton in the south and with upright folds, strike-slip faults, and intense crustal-melting plutonism in NCD and AYD (Figure 2; [67,68,72,83,138]. This is consistent with the age of rare-element leucogranite of MSP in this study, which is emplaced as a laccolith in micaschists.

5.3. Comparison with Pan-African Rare-Metal Granite and Pegmatite

In Africa, Melcher et al. [45] have distinguished five metallogenetic epochs from Archean to Phanerozoic times that are based on mineralogical and geochemical features of the rare-metal minerals (Figure 1). With its U-Pb age on columbo-tantalite and monazite at ca. 600–580 Ma, the Nb-Ta-Sn mineralization of the Mayo Salah pluton can be associated with the youngest period: the late-Neoproterozoic to early-Paleozoic, designated as Pan-African ca. 600 to 450 Ma, when numerous mineralized pegmatites are described within Pan-African mobile belts that were surrounding the cratons e.g., Arabian-Nubian Shield, Mozambique Belt, and Damara Belt in Namibia (Figure 1; [58–60]).

Current occurrences of Pan-African rare-metal granites are restricted to the Older Granites and Younger Granites of Nigeria; and the granites of Eastern Desert of Egypt in the Arabian–Nubian Shield (ANS). The ANS constitutes the northern part of the East African Orogenic Belt and the rare-metal mineralization is associated with a post-accretionary magmatic phase ranging in age from ca. 610 Ma in the north to ca. 530 Ma in the south [53]. In Nigeria, the Older granite is late Neoproterozoic and Younger Granites are Mesozoic [45]. The mineralization of the Mayo Salah leucogranite (Mn-columbite) is similar to the RMG of the Eastern Desert (Egypt) in ANS, especially to the RMG of Abu Dabbad and Nuweibi, which contain zoned CGMs [129] with Ta mineralization mainly as columbite-(Mn) and some tantalite-(Mn) that both have low concentrations of Li and Ti, but high concentrations of Sc, REE, and Th [45]. This study highlights the presence of late-Neoproterozoic rare-metal granite in the CAFB (Figure 1), where the known occurrences are restricted to rare-element pegmatites and RMG of Nigeria [45,46,55].

6. Conclusions

(1) The Mayo Salah pluton shares the features of rare-metal granites RMG with local occurrences of rare-element minerals during the magmatic fractionation of this pluton. Rare-element mineralization (Nb, Ta, and Sn) is expressed as cassiterite and homogeneously disseminated Nb-Ta oxides, such as coltan, rutile, and pyrochlore. The Nb-Ta oxides are classified as Mn-columbite and are magmatic in origin. The progressive zonation of these minerals suggest a magmatic fractionation with earlier Nb-rich Mn-columbite and late Ta-rich Mn columbite. The later stage might be related to magmato-hydrothermal alteration. The rare-element leucogranite of the Mayo Salah pluton is peraluminous and I-type to S-type suggesting an origin from melting of crustal material with a contribution of sediments. The leucogranite of Mayo Salah is classified into the peraluminous low-phosphorus group of RMG.

(2) The LA-ICP-MS U-Pb dating of columbite and monazite yields ages between 603.2 ± 5.3 and 581.6 ± 7.2 Ma, which provide evidence for the genesis of the Nb-Ta occurrences of the Mayo Salah pluton by a late-Neoproterozoic (Pan-African) magmatic event. Structural and geochronological features show that the MSP is related to the late D_2 to syn-tectonic D_3 events that were recorded in the CAFB. The Nb-Ta occurrences of the Mayo Salah pluton can be related to the Pan-African Nb-Ta epoch proposed by [45] ranging from ca. 600 to 450 Ma (late-Neoproterozoic to early-Paleozoic) and that includes Pan-African belts surrounding the Congo Craton as the Central Africa Fold Belt, Mozambique Belt, Damara Belt in Namibia, and the northern part of the East African Orogenic Belt.

Supplementary Materials: The following are available online at http://www.mdpi.com/2075-163X/8/5/188/s1, Table S1: Operating conditions for the LA-ICP-MS equipment, Table S2: Representative electron-microprobe analyses of columbite from the Mayo Salah pluton (MsLF), Table S3: Representative electron-microprobe analyses

of columbite from the Mayo Salah pluton (MsLC), Table S4: Representative electron-microprobe analyses of columbite from the Mayo Salah pluton (MsLCm).

Author Contributions: Conception of the project, R.T.; Field work, R.T., P.M.F.T., N.S.F. and E.N.N; Petrography, H.S.D. and P.M.F.T.; Geochemistry preparation and treatment, P.M.F.T., H.S.D. and A.-S.A.-M.; E.P.M.A. analyses, P.M.F.T. and O.R.; LA-ICP-MS U-Pb dating analysis and treatment, M.P., H.S.D., F.T. and P.M.F.T.; Writing—Original Draft, P.M.F.T, F.T., H.S.D., A.-S.A.-M and R.T.; Writing—Review & Editing, P.M.F.T., F.T., A.-S.A.-M. and R.T.; Supervision, A.-S.A.-M. and R.T.; Funding Acquisition, R.T. and A.-S.A.-M.

Acknowledgments: This manuscript is a part of the Ph.D. of the first author. The authors thank the AUA (Association des Universités Africaines) for financial support of fieldtrips in Cameroon. We thank the Embassy of France in Cameroon for scholarships and financial supports, for six-month stay in France in the GeoRessources laboratory of Université de Lorraine-CNRS, Nancy, to perform the analytical work of this study. This work was funded by the Labex Ressources 21 (supported by the French National Research Agency—France) through the national program "Investissements d'avenir", reference ANR-10-LABX-21–LABEX RESSOURCES 21. Thanks to Alexandre Flammang and Moine John for her helps during thin sections preparation, and Lise Salsi for BSE images acquisition.

Conflicts of Interest: The authors declare no conflict of interest.

References

1. Chakhmouradian, A.R. High-field-strength elements in carbonatitic rocks: Geochemistry, crystal chemistry and significance for constraining the sources of carbonatites. *Chem. Geol.* **2006**, *235*, 138–160. [CrossRef]
2. Linnen, R.L.; Van Lichtervelde, M.; Černý, P. Granitic pegmatites: Granitic pegmatites as sources of strategic metals. *Elements* **2012**, *8*, 275–280. [CrossRef]
3. Linnen, R.L.; Samson, I.M.; Williams-Jones, A.E.; Chakhmouradian, A.R. Geochemistry of the rare-earth element, Nb, Ta, Hf, and Zr deposits. In *Treatise on Geochemistry*, 2nd ed.; Heinrich, D.H., Andrew, M.D., Eds.; Elsevier Science: New York, NY, USA, 2014; Volume 13, pp. 543–568.
4. Linnen, R.L.; Cuney, M. Granite-related rare-element deposits and experimental constraints on Ta-Nb-W-Sn-Zr-Hf mineralization. In *Rare-Element Geochemistry and Mineral Deposits*; Linnen, R.L., Samson, I.M., Eds.; Short Course Notes; Geological Association of Canada: St. John's, NL, Canada, 2005; Volume 17, pp. 45–68.
5. Dostal, J. Rare earth element deposits of alkaline igneous rocks. *Resources* **2017**, *6*, 34. [CrossRef]
6. Cuney, M.; Marignac, C.; Weisbrod, A. The Beauvoir topaz–lepidolite albite granite (Massif Central, France); the disseminated magmatic Sn-Li-Ta-Nb-Be mineralization. *Econ. Geol.* **1992**, *87*, 1766–1794. [CrossRef]
7. Fouillac, A.M.; Rossi, P. Near-solidus δ18 O depletion in a Ta-Nb-bearing albite granite: The Beauvoir granite, France. *Econ. Geol.* **1991**, *86*, 1704–1720. [CrossRef]
8. Wang, R.C.; Fontan, F.; Monchoux, P. Minéraux disséminés comme indicateurs du caractère pegmatitique du granite de Beauvoir, Massif d'Echassières, allier, France. *Can. Mineral.* **1992**, *30*, 763–770.
9. Belkasmi, M.; Cuney, M.; Pollard, P.J.; Bastoul, A. Chemistry of the Ta-Nb-Sn-W oxide minerals from the Yichun rare metal granite (SE China): Genetic implications and comparison with Moroccan and French Hercynian examples. *Mineral. Mag.* **2000**, *64*, 507–523. [CrossRef]
10. Huang, X.L.; Wang, R.C.; Chen, X.M.; Hu, H.; Liu, C.S. Vertical variations in the mineralogy of the Yichun topaz–lepidolite granite, Jiangxi Province, southern China. *Can. Mineral.* **2002**, *40*, 1047–1068. [CrossRef]
11. Breiter, K.; Škoda, R.; Uher, P. Nb–Ta–Ti–W–Sn–oxide minerals as indicators of a peraluminous P- and F-rich granitic system evolution: Podlesí, Czech Republic. *Mineral. Petrol.* **2007**, *91*, 225–248. [CrossRef]
12. René, M.; Škoda, R. Nb-Ta-Ti oxides fractionation in rare-metal granites: Krásno-Horní Slavkov ore district, Czech Republic. *Mineral. Petrol.* **2011**, *103*, 37–48. [CrossRef]
13. Rao, C.; Wang, R.C.; Hu, H.; Zhang, W.L. Complex internal textures in oxide minerals from the Nanping No. 31 dyke of granitic pegmatite, Fujian province, southeastern China. *Can. Mineral.* **2009**, *47*, 1195–1212. [CrossRef]
14. Xie, L.; Wang, R.C.; Che, X.D.; Huang, F.F.; Erdmann, S.; Zhang, W.-L. Tracking magmatic and hydrothermal Nb–Ta–W–Sn fractionation using mineral textures and composition: A case study from the late Cretaceous Jiepailing ore district in the Nanling Range in South China. *Ore Geol. Rev.* **2016**, *78*, 300–321. [CrossRef]
15. Zhu, Z.Y.; Wang, R.C.; Che, X.D.; Zhu, J.C.; Wei, X.L.; Huang, X.E. Magmatic–hydrothermal rare-element mineralization in the Songshugang granite (northeastern Jiangxi, China): Insights from an electron-microprobe study of Nb–Ta–Zr minerals. *Ore Geol. Rev.* **2015**, *65*, 749–760. [CrossRef]

16. Kovalenko, V.I. The genesis of rare metal granitoids and related ore deposits. In *Metallization Associated with Acid Magmatism*; Štemprok, M.B., Tischendorf, G., Eds.; Geological Survey: Prague, Czech Republic, 1978; Volume 3, pp. 235–258.
17. Eby, G.N. Chemical subdivision of the A type granitoids: Petrogenetic and tectonic implications. *Geology* **1992**, *20*, 641–644. [CrossRef]
18. Ishihara, S. The granitoids series and mineralization. *Econ. Geol.* **1981**, *75*, 458–484.
19. White, A.J.R.; Chappell, B.W. Ultrametamorphism and granite genesis. *Tectonophysics* **1977**, *43*, 7–22. [CrossRef]
20. Černý, P.; Ercit, T.S. Some recent advances in the mineralogy and geochemistry of Nb and Ta in rare-element granitic pegmatites. *Bull. Minerai* **1985**, *108*, 499–532.
21. Turlin, F.; André-Mayer, A.-S.; Moukhsil, A.; Vanderhaeghe, O.; Gervais, F.; Solgadi, F.; Groulier, P.-A.; Poujol, M. Unusual LREE-rich, peraluminous, monazite- or allanite-bearing pegmatitic granite in the central Grenville Province, Québec. *Ore Geol. Rev.* **2017**, *89*, 627–667. [CrossRef]
22. Ballouard, C.; Poujol, M.; Boulvais, P.; Branquet, Y.; Tartèse, R.; Vigneresse, J.-L. Nb-Ta fractionation in peraluminous granites: A marker of the magmatic-hydrothermal transition. *Geology* **2016**, *44*, 231–234. [CrossRef]
23. Černý, P. Petrogenesis of granitic pegmatites. In *Granitic Pegmatites in Science and Industry*; Černý, P., Ed.; Short Course Handbook; Mineralogical Association of Canada: Québec City, QC, Canada, 1982; Volume 8, pp. 405–461.
24. Černý, P.; Ercit, T.S. Mineralogy of niobium and tantalum: Crystal chemical relationships, paragenetic aspects and their economic implications. In *Lanthanides, Tantalum and Niobium*; Möller, P., Černý, P., Saupé, F., Eds.; Springer Verlag: Berlin Heidelberg, Germany, 1989; pp. 27–79.
25. Černý, P.; Blevin, P.L.; Cuney, M.; London, D. Granite-related ore deposits. *Econ. Geol.* **2005**, *100*, 337–370.
26. Ercit, T.S. REE-enriched granitic pegmatites. In *Rare-Element Geochemistry and Mineral Deposits*; Linnen, R.L., Samson, I.M., Eds.; Short Course Notes; Geological Association of Canada: St. John's, NL, Canada, 2005; Volume 17, pp. 175–199.
27. Tadesse, S.; Zerihun, D. Composition, fractionation trend and zoning accretion of the columbite–tantalite group of minerals in the Kenticha rare metal field (Adola, southern Ethiopia). *J. Afr. Earth Sci.* **1996**, *23*, 411–431. [CrossRef]
28. Van Lichtervelde, M.; Salvi, S.; Beziat, D.; Linnen, R.L. Textural features and chemical evolution in tantalum oxides; magmatic versus hydrothermal origins for Ta mineralization in the Tanco lower pegmatite, Manitoba, Canada. *Econ. Geol.* **2007**, *102*, 257–276. [CrossRef]
29. Van Lichtervelde, M.; Holtz, F.; Hanchar, J.M. Solubility of manganotantalite, zircon and hafnon in highly fluxed peralkaline to peraluminous pegmatitic melts. *Contrib. Mineral. Petrol.* **2010**, *160*, 17–32. [CrossRef]
30. Breiter, K.; Škoda, R. Vertical zonality of fractionated granite plutons refected in zircon chemistry: The Cínovec A-type versus the Beauvoir S-type suite. *Geol. Carpath.* **2012**, *63*, 383–398. [CrossRef]
31. Černý, P.; Goad, B.E.; Hawthorne, F.C.; Chapman, R. Fractionation trends of the Nb and Ta-bearing oxide minerals in the Greer Lake pegmatitic granite and its pegmatite aureole, southeastern Manitoba. *Am. Mineral.* **1986**, *71*, 501–517.
32. Harlaux, M.; Marignac, C.; Cuney, M.; Mercadier, J.; Magott, R.; Mouthier, B. Nb-Ti-Y-HREE-W-U oxide minerals with uncommon compositions associated with the tungsten mineralization in the Puy-les-Vignes deposit (Massif central, France): Evidence for rare-metal mobilization by late hydrothermal fluids with a peralkaline signature. *Can. Mineral.* **2015**, *53*, 653–672. [CrossRef]
33. Harlaux, M.; Romer, R.L.; Mercadier, J.; Morlot, C.; Marignac, C.; Cuney, M. 40 Ma of hydrothermal W mineralization during the Variscan orogenic evolution of the French Massif Central revealed by U-Pb dating of wolframite. *Miner. Depos.* **2017**, *53*, 21–51. [CrossRef]
34. Lerouge, C.; Gloaguen, W.G.; Bailly, L. Distribution of In and other rare metals in cassiterite and associated minerals in Sn, W ore deposits of the western Variscan Belt. *Eur. J. Mineral.* **2017**, *29*, 739–753. [CrossRef]
35. Wang, R.C.; Hu, H.; Zhang, A.C. Pollucite and the cesium-dominant analogue of polylithionite as expressions of extreme Cs enrichment in the Yichun topaz-lepidolithe granite, Southern China. *Can. Mineral.* **2004**, *42*, 883–896. [CrossRef]
36. Linnen, R.L. The solubility of Nb-Ta-Zr-Hf-Win granitic melts with Li and Li + F: Constraints for mineralization in rare metal granites and pegmatites. *Econ. Geol.* **1998**, *93*, 1013–1025. [CrossRef]

37. Linnen, R.L.; Keppler, H. Columbite solubility in granitic melts; consequences for the enrichment and fractionation of Nb and Ta in the Earth's crust. *Contrib. Mineral. Petrol.* **1997**, *128*, 213–227. [CrossRef]
38. Tiepolo, M.; Bottazzi, P.; Foley, S.F.; Oberti, R.; Vannucci, R.; Zanetti, A. Fractionation of Nb and Ta from Zr and Hf at mantle depths: The role of titanian pargasite and kaersutite. *J. Petrol.* **2001**, *42*, 221–232. [CrossRef]
39. Salvi, S.; Williams-Jones, A.E. Alkaline granite-syenite hosted deposits. In *Rare Element Geochemistry and Mineral Deposits*; Linnen, R.L., Samson, I.M., Eds.; Short Course Notes; Geological Association of Canada: St. John's, NL, Canada, 2005; Volume 17, pp. 315–341.
40. Dill, H.G. Pegmatite and aplites: Their genetic and applied ore geology. *Ore Geol. Rev.* **2015**, *65*, 417–561. [CrossRef]
41. Aseri, A.A.; Linnen, R.L.; Che, X.D.; Yves, T.; Francois, H. Effects of fluorine on the solubilities of Nb, Ta, Zr and Hf minerals in highly fluxed water-saturated haplogranitic melts. *Ore Geol. Rev.* **2015**, *64*, 736–746. [CrossRef]
42. Fiege, A.; Kirchner, C.; Holtz, F.; Linnen, R.L.; Dziony, W. Influence of fluorine on the solubility of manganotantalite ($MnTa_2O_6$) and manganocolumbite ($MnNb_2O_6$) in granitic melts—An experimental study. *Lithos* **2011**, *122*, 165–174. [CrossRef]
43. Keppler, H. Influence of fluorine on the enrichment of high field strength trace elements in granitic rocks. *Contrib. Mineral. Petrol.* **1993**, *114*, 479–488. [CrossRef]
44. Deschamps, Y.; Hocquard, C.; Pelon, R.; Milési, J.P.; Ralay, F. *Geology and Ta Ore Deposits (Africa)*; BRGM: Orléans, France, 2006; Map 1:10,000,000.
45. Melcher, F.; Graupner, T.; Gäbler, H.-E.; Sitnikova, M.; Henjes-Kunst, F.; Oberthür, T.; Gerdes, A.; Dewaele, S. Tantalum-(niobium-tin) mineralisation in African pegmatites and rare metal granites: Constraints from Ta-Nb oxide mineralogy, geochemistry and U-Pb geochronology. *Ore Geol. Rev.* **2015**, *64*, 667–719. [CrossRef]
46. Akoh, J.U.; Ogunleye, P.O.; Ibrahim, A.A. Geochemical evolution of micas and Sn-, Nb-, Ta-mineralization associated with the rare metal pegmatite in Angwan Doka, central Nigeria. *J. Afr. Earth Sci.* **2015**, *112*, 24–36. [CrossRef]
47. Dewaele, S.; De Clerq, F.; Muchez, P.; Schneider, J.; Burgess, R.; Boyce, A.; Fernandez-Alonso, M. Geology of the cassiterite mineralisation in the Rutongo area, Rwanda (Central Africa): Current state of knowledge. *Geol. Belgica* **2010**, *13*, 91–112.
48. Dewaele, S.; Henjes-Kunst, F.; Melcher, F.; Sitnikova, M.; Burgess, R.; Gerdes, A.; Fernandez-Alonso, M.; De Clerq, F.; Muchez, P.; Lehmann, B. Late Neoproterozoic overprinting of the cassiterite and columbite–tantalite bearing pegmatites of the Gatumba area, Rwanda (Central Africa). *J. Afr. Earth Sci.* **2011**, *61*, 10–26. [CrossRef]
49. Dewaele, S.; Hulsbosch, N.; Cryns, Y.; Boyce, A.; Burgess, R.; Muchez, P. Geological setting and timing of the world-class Sn, Nb–Ta and Li mineralization of Manono-Kitotolo (Katanga, Democratic Republic of Congo). *Ore Geol. Rev.* **2015**, *72*, 373–390. [CrossRef]
50. Diehl, M. Rare metal pegmatites of the Cape Cross-Uis pegmatite belt, Namibia: Geology, mineralisation, rubidium-strontium characteristics and petrogenesis. *J. Afr. Earth Sci.* **1993**, *17*, 167–181. [CrossRef]
51. Hulsbosch, N.; Hertogen, J.; Dewaele, S.; Andre, L.; Muchez, P. Petrographic and mineralogical characterisation of fractionated pegmatites culminating in the Nb-Ta-Sn pegmatites of the Gatumba area (western Rwanda). *Geol. Belgica* **2013**, *16*, 105–117.
52. Küster, D. Rare-metal pegmatites of Wamba, central Nigeria—Their formation in relationship to late Pan-African granites. *Miner. Depos.* **1990**, *25*, 25–33. [CrossRef]
53. Küster, D. Granitoid-hosted Ta mineralization in the Arabian–Nubian Shield: Ore deposit types, tectono-metallogenetic setting and petrogenetic framework. *Ore Geol. Rev.* **2009**, *35*, 68–86. [CrossRef]
54. Milési, P.; Toteu, S.F.; Deschamps, Y.; Feybesse, J.L.; Lerouge, C.; Cocherie, A.; Penaye, J.; Tchameni, R.; Moloto-A-Kenguemba, G.; Kampubzu, H.A.B.; et al. An overview of the geology and major ore deposits of Central Africa: Explanatory note for the 1:4,000,000 map "Geology and major ore deposits of Central Africa". *J. Afr. Earth Sci.* **2006**, *44*, 571–595. [CrossRef]
55. Ogunleye, P.O.; Garba, I.; Ike, E.C. Factors contributing to enrichment and crystallization of niobium in pyrochlore in the Kaffo albite arfvedsonite granite, Ririwai Complex, Younger Granites province of Nigeria. *J. Afr. Earth Sci.* **2006**, *44*, 372–382. [CrossRef]
56. Pohl, W. Metallogeny of the northeastern Kibara belt, Central Africa—Recent perspectives. *Miner. Depos.* **1994**, *9*, 105–130. [CrossRef]

57. Decrée, S.; Boulvais, P.; Cobert, C.; Baele, J.M.; Midende, G.; Gardien, V.; Tack, L. Structurally-controlled hydrothermal alteration in the syntectonic Neoproterozoic Upper Ruvubu Alkaline Plutonic Complex (Burundi): Implications for REE and HFSE. *Precambrian Res.* **2015**, *269*, 281–295. [CrossRef]
58. De Wit, M.J.; Stankiewicz, J.; Reeves, C. *Restoring Pan-African-Brasiliano Connections: More Gondwana Control, Less Trans-Atlantic Corruption*; The Geological Society London: London, UK, 2008; Volume 294, pp. 399–412. [CrossRef]
59. Allen, P.A. The Huqf Supergroup of Oman: Basin development and context for Neoproterozoic glaciation. *Earth-Sci. Rev.* **2007**, *84*, 139–185. [CrossRef]
60. Kröner, A.; Stern, R.J. Africa: Pan-African orogeny. In *Encyclopedia of Geology*; Elsevier: Amsterdam, The Netherlands, 2004; Volume 1, pp. 1–12.
61. Bouyo Houketchang, M.; Penaye, J.; Barbey, P.; Toteu, S.F.; Wandji, P. Petrology of high-pressure granulite facies metapelites and metabasites from Tchollirée and Banyo regions: Geodynamic implication for the Central African Fold Belt (CAFB) of north-central Cameroon. *Precambrian Res.* **2013**, *224*, 412–433. [CrossRef]
62. Bouyo Houketchang, M.; Zhao, Y.; Penaye, J.; Zhang, S.H.; Njel, U.O. Neoproterozoic subduction-related metavolcanic and metasedimentary rocks from the Rey Bouba Greenstone Belt of north-central Cameroon in the Central African Fold Belt: New insights into a continental arc geodynamic setting. *Precambrian Res.* **2015**, *261*, 40–53. [CrossRef]
63. Bouyo Houketchang, M.; Penaye, J.; Njel, U.O.; Moussango, A.P.I.; Sep, J.P.N.; Nyama, B.A.; Wassouo, W.J.; Abate, J.M.E.; Yaya, F.; Mahamat, A.; et al. Geochronological, geochemical and mineralogical constraints of emplacement depth of TTG suite from the Sinassi Batholith in the Central African Fold Belt (CAFB) of northern Cameroon: Implications for tectonomagmatic evolution. *J. Afr. Earth Sci.* **2016**, *116*, 9–41. [CrossRef]
64. Ngako, V.; Affaton, P.; Njonfang, E. Pan-African tectonics in northwestern Cameroon: Implication for the history of western Gondwana. *Gondwana Res.* **2008**, *14*, 509–522. [CrossRef]
65. Negue, N.E.; Tchameni, R.; Vanderhaeghe, O.; Barbey, P.; Tchunte, P.M.F.; Takodjou, W.J.D.; Lemdjou, B.Y.; Saha, F.A.N. Petrography and geochemistry of the Mbip Granitic Massif, SW Tchollirée (Central North Cameroon): Petrogenetic and geodynamic implication. *Int. J. Geosci.* **2015**, *6*, 761–775. [CrossRef]
66. Negue, N.E.; Tchameni, R.; Vanderhaeghe, O.; Fenguye, S.; Barbey, P.; Tekoum, L.; Eglinger, A.; Fosso Tchunte, P.M.; Saha, F.A.N. Structure and LA-ICP-MS zircon U-Pb dating of syntectonic plutons emplaced in the Pan-African Banyo-Tcholliré shear zone (central north Cameroon). *J. Afr. Earth Sci.* **2017**, *131*, 251–271.
67. Penaye, J.; Kröner, A.; Toteu, S.F.; Van Schmus, W.R.; Doumnang, J.-C. Evolution of the Mayo Kebbi region as revealed by zircon dating: An early (ca. 740 Ma) Pan-African magmatic arc in southwestern Chad. *J. Afr. Earth Sci.* **2006**, *44*, 530–542. [CrossRef]
68. Toteu, S.F.; Van Schmus, R.W.; Penaye, J.; Michard, A. New U-Pb and Sm-Nd data from north-central Cameroon and its bearing on the pre-Pan-African history of central Africa. *Precambrian Res.* **2001**, *108*, 45–73. [CrossRef]
69. Toteu, S.F.; Penaye, J.; Poudjom Djomani, Y. Geodynamic evolution of the Pan-African belt in central Africa with special reference to Cameroon. *Can. J. Earth Sci.* **2004**, *41*, 73–85. [CrossRef]
70. Toteu, S.F.; Penaye, J.; Deloule, E.; Van Schmus, W.R.; Tchameni, R. Diachronous evolution of volcano-sedimentary basins north of the Congo craton: Insights from U-Pb ion microprobe dating of zircons from the Poli, Lom and Yaoundé groups (Cameroon). *J. Afr. Earth Sci.* **2006a**, *44*, 428–442. [CrossRef]
71. Le Fur, Y. Section 2: Géologie Appliquée, chronique des mines. In *Les Indices de cuivre du Groupe Volcano-Sédimentaire de Poli (Cameroun)*; Bureau de Recherches Géologiques et Minières: Orléans, France, 1971; Volume 6, p. 79.
72. Isseini, M.; André-Mayer, A.S.; Vanderhaeghe, O.; Barbey, P.; Deloule, E. A-type granites from the Pan-African orogenic belt in south-western Chad constrained using geochemistry, Sr-Nd isotopes and U-Pb geochronology. *Lithos* **2012**, *153*, 39–52. [CrossRef]
73. Kouske, A.P.; Suh, C.E.; Ghogomu, R.T.; Ngako, V. Na-Metasomatism and Uranium Mineralization during a Two-Stage Albitization at Kitongo, Northern Cameroon: Structural and Geochemical Evidence. *Int. J. Geosci.* **2012**, *3*, 258–279. [CrossRef]
74. Kusnir, I. *Géologie, Ressources Minérales et Ressources en eau du Tchad*, 2nd ed.; CNAR: Ndjaména, Chad, 1995; p. 116.
75. Mbaguedje, D. Métallogénie de l'or et de L'uranium dans le Cadre de la Croissance et de la Différenciation de la Croûte au Néoprotérozoïque: Exemple du Massif du Mayo-Kebbi (Tchad) dans la Ceinture Orogénique d'Afrique Centrale. Ph.D. Thesis, Université de Lorraine, GeoRessources-CREGU, Lorraine, France, 2015.

76. Oesterlen, M.; Vetter, U. *Petrographic-Geochemical Characteristics and Genesis of an Albitized Uraniferous Granite in Northern Cameroon, Africa. Vein Type Uranium Deposits*; Technical Document; International Atomic Energy Agency: Vienna, Austria, 1986; Volume 361, pp. 113–142.
77. Pinna, P.; Edimo, A.; Jézéquel, J.; Tchountchoui, D.; Ebotayuk-Ebop, M. *Inventaire Minier du Centre-Nord Cameroun (Troisième Phase)*; Open-File Report 88 CMR 168; BRGM: Orléans, France, 1989.
78. Vels, B.; Fritsche, R. Sodium metasomatism in the Kitongo uranium occurrence near Poli, Cameroon. *Uranium* **1988**, *4*, 365–383.
79. Toteu, S.F. Geochemical characterization of the main petrographical and structural units of northern Cameroon: Implications for Pan-African evolution. *J. Afr. Earth Sci.* **1990**, *10*, 615–624. [CrossRef]
80. Abdelsalam, M.G.; Liégeois, J.P.; Stern, R.J. The Saharan metacraton. *J. Afr. Earth Sci.* **2002**, *34*, 119–136. [CrossRef]
81. Abdelsalam, M.G.; Gao, S.S.; Liégeois, J.-P. Upper mantle structure of the Saharan Metacraton. *J. Afr. Earth Sci.* **2011**, *60*, 328–336. [CrossRef]
82. Bouyo Houketchang, M.; Toteu, S.F.; Deloule, E.; Penaye, J.; Van Schmus, W.R. U-Pb and Sm-Nd dating of high-pressure granulites from Tchollirée and Banyo regions: Evidence for a Pan-African granulite facies metamorphism in northcentral Cameroon. *J. Afr. Earth Sci.* **2009**, *54*, 144–154. [CrossRef]
83. Dawaï, D.; Bouchez, J.-L.; Paquette, J.-L.; Tchameni, R. The Pan-African quartz-syenite of guider (north-Cameroon): Magnetic fabric and U-Pb dating of a late orogenic emplacement. *Precambrian Res.* **2013**, *236*, 132–144. [CrossRef]
84. Tchameni, R.; Sun, F.; Dawaï, D.; Danra, G.; Tékoum, L.; Negue, N.E.; Vanderhaeghe, O.; Nzolang, C.; Dagwaï, N. Zircon dating and mineralogy of the Mokong Pan-African magmatic epidote-bearing granite (North Cameroon). *Int. J. Earth Sci.* **2016**, *105*, 1811–1830. [CrossRef]
85. Ganwa, A.A.; Frisch, W.; Siebel, W.; Ekodeck, G.E.; Kongnyuy, C.; Ngako, V. Archean inheritances in the pyroxene-amphibole-bearing gneiss of the Méiganga area (Central North Cameroon): Geochemical and 207Pb/206Pb age imprints. *C.R. Geosci.* **2008**, *340*, 211–222. [CrossRef]
86. Ganwa, A.A.; Klötzli, S.U.; Hauzenberger, C. Evidence for Archean inheritance in the pre-Panafrican crust of Central Cameroon: Insight from zircon internal structure and LA-MC-ICP-MS U-Pb ages. *J. Afr. Earth Sci.* **2016**, *120*, 12–22. [CrossRef]
87. Penaye, J.; Toteu, S.F.; Tchameni, R.; Van Schmus, W.R.; Tchakounte, J.; Ganwa, A.A.; Minyem, D.; Nsifa, E.N. The 2.1 Ga West Central African belt in Cameroon: Extension and evolution. *J. Afr. Earth Sci.* **2004**, *39*, 159–164. [CrossRef]
88. Doumnang, J.-C. Géologie des Formations Néoprotérozoïques du Mayo Kebbi (Sud-Ouest du Tchad): Apports de la Pétrologie et de la Géochimie, Implications sur la Géodynamique au Panafricain. Ph.D. Thesis, Université d'Orléans, Orléans, France, 2006.
89. Ngako, V.; Jégouzo, P.; Soba, D. Déformation et métamorphisme dans la chaîne panafricaine de Poli (Nord Cameroun): Implications géodynamiques et paléogéographiques. *J. Afr. Earth Sci.* **1989**, *9*, 541–555. [CrossRef]
90. Njel, U.O. Paléogéographie d'un segment de l'orogenèse panafricaine: La ceinture volcano-sédimentaire de Poli (Nord Cameroun). *C.R. Acad. Sci. Paris* **1986**, *303*, 1737–1742.
91. Pinna, P.; Calvez, J.-Y.; Abessolo, A.; Angel, J.-M.; Mekoulou-Mekoulou, T.; Mananga, G.; Vernhet, Y. Neoproterozoic events in the Tcholliré area: Pan-African crustal growth and geodynamics in central-northern Cameroon (Adamawa and North Provinces). *J. Afr. Earth Sci.* **1994**, *18*, 347–353. [CrossRef]
92. Pouclet, A.; Vidal, M.; Doumnang, J.-C.; Vicat, J.-P.; Tchameni, R. Neoproterozoic crustal evolution in Southern Chad: Pan-African ocean basin closing, arc accretion and late- to post-orogenic granitic intrusion. *J. Afr. Earth Sci.* **2006**, *44*, 543–560. [CrossRef]
93. Penaye, J.; Toteu, S.F.; Michard, A.; Bertrand, J.M.; Dautel, D. Reliques granulitiques d'âge Protérozoïque inférieur dans la zone mobile panafricaine d'Afrique Centrale au Cameroun; géochronologie U-Pb sur zircons. *C.R. Acad. Sci. Paris* **1989**, *309*, 315–318.
94. Toteu, S.F.; Michard, A.; Bertrand, J.M.; Rocci, G. U-Pb dating of Precambrian rocks from northern Cameroon, orogenic evolution and chronology of the Pan-African belt of central Africa. *Precambrian Res.* **1987**, *37*, 71–87. [CrossRef]

95. Ngako, V. *Evolution Métamorphique et Structurale de la Bordure Sud-Ouest de la «Série de Poli». (Segment Camerounais de la Chaine Pan-Africaine)*; Mémoires et Documents du C.A.E.S.S. No. 5; C.A.E.S.S.: Rennes, France, 1986; p. 185.
96. Toteu, S.F.; Michard, A.; Macaudière, J.; Bertrand, J.-M.; Penaye, J. Données géochronologiques nouvelles (U/Pb et Rb/Sr) sur la zone mobile pan-africaine du Nord Cameroun. *C.R. Acad. Sci. Paris* **1986**, *303*, 375–378.
97. Carignan, J.; Hold, P.; Mevelle, G.; Morel, J.; Yeghichevan, D. Routine analysis of trace elements in geological samples using flow injection and low pressure on line liquid chromatography coupled to ICP-MS: A study of geochemical reference materials BR, DRN, UB-N, AN-G and GH. *Geostand. Geoanal. Res.* **2001**, *25*, 187–198. [CrossRef]
98. Ballouard, C.; Boulvais, P.; Poujol, M.; Gapais, D.; Yamato, P.; Tartèse, R.; Cuney, M. Tectonic record, magmatic history and hydrothermal alteration in the Hercynian Guérande leucogranite, Armorican Massif, France. *Lithos* **2015**, *220–223*, 1–22. [CrossRef]
99. Jackson, S.E.; Pearson, N.J.; Griffin, W.L.; Belousova, E.A. The application of laser ablation-inductively coupled plasma-mass spectrometry to in situ U-Pb zircon geochronology. *Chem. Geol.* **2004**, *211*, 47–69. [CrossRef]
100. Gasquet, D.; Bertrand, J.-M.; Paquette, J.-L.; Lehmann, J.; Ratzov, G.; Guedes, R.D.A.; Tiepolo, M.; Boullier, A.-M.; Scaillet, S.; Nomade, S. Miocene to Messinian deformation and hydrothermal activity in a pre-Alpine basement massif of the French western Alps: New U–U–Th–Pb and argon ages from the Lauzière massif. *Bull. Soc. Geol. Fr.* **2010**, *181*, 227–241. [CrossRef]
101. Wiedenbeck, M.; Allé, P.; Corfu, F.; Griffin, W.L.; Meier, M.; Oberli, F.; Quadt, A.V.; Roddick, J.C.; Spiegel, W. Three natural zircon standards for U–Th–Pb, Lu–Hf, trace element and REE analyses. *Geostand. Geoanal. Res.* **1995**, *19*, 1–23. [CrossRef]
102. Paquette, J.L.; Tiepolo, M. High resolution (5 μm) U–Th–Pb isotope dating of monazite with excimer laser ablation (ELA)-ICPMS. *Chem. Geol.* **2007**, *240*, 222–237. [CrossRef]
103. Van Achterbergh, E.; Ryan, C.G.; Jackson, S.E.; Griffin, W.L. Data reduction software for LA-ICPMS: Appendix. In *Laser Ablation-ICP Mass Spectrometry in the Earth Sciences: Principles and Applications*; Sylvester, P.J., Ed.; Mineralogical Association of Canada (MAC) Short Courses Ser.: Ottawa, ON, Canada, 2001; Volume 29, pp. 239–243.
104. Ludwig, K.R. *Isoplot/Ex Version 2.49. A Geochronological Toolkit for Microsoft Excel*; Special Publication 1; Berkeley Geochronology Center: Berkeley, CA, USA, 2001; pp. 1–55.
105. Lahti, S.I. Zoning in columbite-tantalite crystals from the granitic pegmatites of the Eräjärvi area, southern Finland. *Geochim. Cosmochim. Acta* **1987**, *51*, 509–517. [CrossRef]
106. Atencio, D.; de Andrade, M.B.; Christy, A.G.; Giere, R.; Kartashev, P.M. The pyrochlore supergroup of minerals: Nomenclature. *Can. Mineral.* **2010**, *48*, 673–698. [CrossRef]
107. Middlemost, E.A.K. Naming material in the magma/igneous rock system. *Earth-Sci. Rev.* **1994**, *37*, 215–224. [CrossRef]
108. Irvine, T.N.; Baragar, W.R.A. A guide to the chemical classification of the common volcanic rocks. *Can. J. Earth Sci.* **1971**, *8*, 523–548. [CrossRef]
109. Shand, S. *Eruptive Rocks. Their Genesis, Composition, Classification, and Their Relations to Ore-Deposits 2*; Wiley: New York, NY, USA, 1943; p. 444.
110. Debon, F.; Lefort, P. A cationic classification of common plutonic rocks and their magmatic associations: Principles, method, applications. *Bull. Minéral.* **1988**, *111*, 493–510.
111. Cuney, M. Felsic magmatism and uranium deposits. *Bull. Soc. Géol. Fr.* **2014**, *185*, 75–92. [CrossRef]
112. Cuney, M.; Friedrich, M.; Blumenfeld, P.; Bourguignon, A.; Boiron, M.C.; Vigneresse, J.L.; Poty, B. Metallogenesis in the French part of the Variscan orogen. Part I: U-preconcentrations in the pre-Variscan and Variscan formations—A comparison with Sn, W and Au. *Tectonophysics* **1989**, *177*, 39–57. [CrossRef]
113. Sun, S.-S.; McDonough, W.F. Chemical and isotopic systematics of oceanic basalts: Implications for mantle composition and processes. In *Magmatism in the Ocean Basins*; Saunders, A.D., Norry, M.J., Eds.; Geological Society of London: London, UK, 1989; Volume 42, pp. 313–345.
114. Taylor, S.R.; McLennan, S.M. The geochemical evolution of the continental crust. *Rev. Geophys.* **1995**, *33*, 241–265. [CrossRef]

115. Turpin, L.; Cuney, M.; Friedrich, M.; Bouchez, J.-L.; Aubertin, M. Meta-igneous origin of Hercynian peraluminous granites in NW French Massif Central: Implications for crustal history reconstructions. *Contrib. Mineral. Petrol.* **1989**, *104*, 163–172. [CrossRef]
116. Bea, F. Residence of REE, Y, Th and U in granites and crustal protoliths; implications for the chemistry of crustal melts. *J. Petrol.* **1996**, *37*, 521–552. [CrossRef]
117. Hönig, S.; Čopjaková, R.; Škoda, R.; Novák, M.; Dolejš, D.; Leichmann, J.; Galiová, M.V. Garnet as a major carrier of the Y and REE in the granitic rocks: An example from the layered anorogenic granite in the Brno Batholith, Czech Republic. *Am. Mineral.* **2014**, *99*, 1922–1941. [CrossRef]
118. Barbarin, B. A review of the relationships between granitoid types, their origins and their geodynamic environments. *Lithos* **1999**, *46*, 605–626. [CrossRef]
119. Wang, R.C.; Fontan, F.; Xu, S.J.; Chen, X.M.; Monchoux, P. The association of columbite, tantalite and tapiolite in the Suzhou granite, China. *Can. Mineral.* **1997**, *35*, 699–706.
120. Cheilletz, A.; Bertrand, J.M.; Charoy, B.; Moulahoum, O.; Bouabsa, L.; Farrar, E.; Zimmermann, J.L.; Dautel, D.; Archibald, D.A.; Boullier, A.M. Géochimie et géochronologie Rb–Sr, K–Ar et 40Ar/39Ar des complexes granitiques pan-africains de la région de Tamanrasset (Algérie); relations avec les minéralisations Sn–W associées et l'évolution tectonique du Hoggar central. *Bull. Soc. Geol. Fr.* **1992**, *163*, 733–750.
121. Rub, A.K.; Štemprok, M.; Rub, M.G. Tantalum mineralization in the apical part of the Cínovec (Zinnwald) granite stock. *Mineral. Petrol.* **1998**, *63*, 199–222. [CrossRef]
122. Breiter, K.; Foerster, H.J.; Seltmann, R. Variscan silicic magmatism and related tin-tungsten mineralization in the Erzgebirge-Slavkovský les metallogenic province. *Miner. Depos.* **1999**, *34*, 505–521. [CrossRef]
123. Förster, H.J.; Rhede, D. The Be-Ta-rich granite of Seiffen (eastern Erzgebirge, Germany): Accessory-mineral chemistry, composition, and age of a late-Variscan Li–F granite of A-type affinity. *J. Mineral. Geochem.* **2006**, *182*, 307–321. [CrossRef]
124. Raimbault, L.; Cuney, M.; Azencott, C.; Duthou, J.L.; Joron, J.L. Geochemical evidence for a multistage magmatic genesis of Ta–Sn–Li mineralization in the granite at Beauvoir, French Massif Central. *Econ. Geol.* **1995**, *90*, 548–576. [CrossRef]
125. Belkasmi, M.; Cuney, M. Les columbo-tantalites zonées du granite de Montebras (Massif central français). Implications petrogénétiques. *C.R. Acad. Sci. Paris* **1998**, *326*, 459–465. [CrossRef]
126. Černý, P.; Meintzer, R.E.; Anderson, A.J. Extreme fractionation in rare element granite pegmatites: Selected examples of data and mechanisms. *Can. Mineral.* **1985**, *23*, 381–421.
127. Huang, F.F.; Wang, R.C.; Xie, L.; Zhu, J.C.; Erdmann, S.; Che, X.D.; Zhang, R.Q. Differentiated rare-element mineralization in an ongonite–topazite composite dike at the Xianghualing tin district, Southern China: An electron-microprobe study on the evolution from niobium–tantalum-oxides to cassiterite. *Ore Geol. Rev.* **2015**, *65*, 761–778. [CrossRef]
128. Tindle, A.G.; Breaks, F.W. Columbite–tantalite mineral chemistry from rare-element granitic pegmatites: Separation Lake area, N.W. Ontario, Canada. *Mineral. Petrol.* **2000**, *70*, 165–198. [CrossRef]
129. Abdalla, H.M.; Helba, H.A.; Mohamed, F.H. Chemistry of columbite–tantalite minerals in rare metal granitoids, Eastern Desert. Egypt. *Mineral. Mag.* **1998**, *62*, 821–836. [CrossRef]
130. Breiter, K. From explosive breccia to unidirectional solidification textures: Magmatic evolution of a phosphorus- and fluorine-rich granite system (Podlesí, Krušné hory Mts.; Czech Republic). *Bull. Czech Geol. Surv.* **2002**, *77*, 67–92.
131. Scott, P.W.; Pascoe, R.D.; Hart, F.W. Columbite-tantalite, rutile and other accessory minerals from the St. Austell topaz granite, Cornwall. *Proc. Ussher Soc.* **1998**, *9*, 165–170.
132. Belkasmi, M.; Cuney, M.; Pollard, P.J. Micas and niobotantalates as indicators of petrogenetic evolution of rare-metal granites. The example of Yashan granitic complex (SE China). In *Lepidolite 200*; Černý, P., Novák, M., Eds.; Masaryk University: Brno, Czech Republic, 1992; pp. 13–14.
133. Wang, R.C. Étude Minéralogique et Cristallochimique de Cassitérite, Niobo-Tantalates et Minéraux Disséminés du Granite de Beauvoir (Allier); Implications Métallogéniques. Ph.D. Thesis, Université Paul Sabatier, Toulouse, France, 1988.
134. Njanko, T.; Nédélec, A.; Kwékam, M.; Siqueira, R.; Esteban, L. Emplacement and deformation of the Fomopéa pluton: Implication for the Pan-African history of Western Cameroon. *J. Struct. Geol.* **2010**, *32*, 306–320. [CrossRef]

135. Ganwa, A.A. Les Granitoïdes de Meiganga: Étude Pétrographique, Géochimique, Structurale et Géochronologique. Leur Place dans la Chaîne Panafricaine. Ph.D. Thesis, Université de. Yaoundé I, Yaoundé, Cameroon, 2005.
136. Van Schmus, W.R.; Oliveira, E.P.; da Silva Filho, A.F.; Toteu, S.F.; Penaye, J.; Guimãraes, I.P. *Proterozoïc Links between the Borborema Province, NE~Brazil, and the Central African Fold Belt*; The Geological Society London: London, UK, 2008; Volume 294, pp. 69–99.
137. Lasserre, M. Données géochronologiques nouvelles acquises au ler Janvier 1967 par la méthode au strontium appliquée aux formations cristallines et cristallophylliennes du Cameroun. *Ann. Fac. Sci.* **1967**, *36*, 109–144.
138. Dawaï, D.; Tchameni, R.; Bascou, J.; Awe, W.S.; Fosso Tchunte, P.M.; Bouchez, J.-L. Microstructures and magnetic fabrics of the Ngaoundéré granite pluton (Cameroon): Implications to the late-Pan-African evolution of Central Cameroon Shear Zone. *J. Afr. Earth Sci.* **2017**, *129*, 887–897. [CrossRef]